Thesis for the degree of licentiate of engineering

Beyond Zero Kelvin: Machine-Learned Potentials for Finite-Temperature Modeling of Semiconductors

Tobias Hainer

Department of Physics and Astronomy
CHALMERS UNIVERSITY OF TECHNOLOGY
Göteborg, Sweden 2026

Beyond Zero Kelvin:
Machine-Learned Potentials for Finite-Temperature Modeling of Semiconductors
Tobias Hainer

© Tobias Hainer, 2026

Department of Physics and Astronomy
Chalmers University of Technology
se-412 96 Göteborg, Sweden
Telephone +46 (0)31 772 10 00

Cover: An artistic rendition of the layered structure found at the morphotropic phase boundary of $MA_{1-x}FA_xPbI_3$.

Chalmers digitaltryck
Göteborg, Sweden 2026

Beyond Zero Kelvin: Machine-Learned Potentials for Finite-Temperature Modeling of Semiconductors

Tobias Hainer
Department of Physics and Astronomy
Chalmers University of Technology

Abstract

The global transition toward sustainable energy sources hinges on the development of efficient, stable and cost-effective photovoltaic materials. Halide perovskites have emerged as leading candidates, with power conversion efficiencies exceeding 25%, yet their operational stability remains a critical bottleneck. Addressing this challenge requires theoretical modeling, but standard density-functional theory (DFT) is largely restricted to zero-kelvin simulations, and extending first-principles methods to finite temperatures remains computationally prohibitive. Machine-learned potentials (MLPs) dramatically reduce this computational cost, enabling finite-temperature simulations at DFT-level accuracy.

This thesis applies this framework to two classes of problems. First, neuroevolution potential (NEP) models are used to decipher the phase diagrams and structural dynamics of the mixed perovskite $MA_{1-x}FA_xPbI_3$, including the identification of a morphotropic phase boundary, and to investigate the debated low-temperature γ-phase of formamidinium lead iodide ($FAPbI_3$). Second, the same framework is extended to the thermodynamics of charged point defects, where thermodynamic integration (TI) is combined with NEP models to evaluate defect formation free energies and charge transition levels as a function of temperature, revealing that thermal effects can substantially shift these quantities across a range of semiconductors.

Taken together, these contributions advance the development of predictive, temperature-aware models of technologically relevant materials, representing a necessary step toward the rational design of stable and efficient next-generation solar cells.

Keywords: perovskites, point defects, charge transition levels, machine-learned interatomic potentials, density functional theory, molecular dynamics, thermodynamic integration, finite-temperature properties, phase transitions

LIST OF APPENDED PAPERS

This thesis is based on work presented in the following papers:

I **A morphotropic phase boundary in $MA_{1-x}FA_xPbI_3$: linking structure, dynamics, and electronic properties**
Tobias Hainer, Erik Fransson, Sangita Dutta, Julia Wiktor, Paul Erhart
Nature Communications **16 (1), 8775**, 2025

II **Revealing the Low-Temperature Phase of $FAPbI_3$ Using a Machine-Learned Potential**
Sangita Dutta, Erik Fransson, **Tobias Hainer**, Benjamin M Gallant, Dominik J Kubicki, Paul Erhart, Julia Wiktor
Journal of the American Chemical Society **147 (41), 37019-37029**, 2025

III **Thermal Stabilization of Defect Charge States and Finite-Temperature Charge Transition Levels**
Tobias Hainer, Ethan Berger, Esmée Berger, Olof Hildeberg, Paul Erhart, Julia Wiktor
Preprint **arXiv:2512.15463**, 2025

The author's contribution to the papers:

I The author performed the molecular dynamics simulations and analysis of these. The author wrote the initial draft of the manuscript, after this the writing was a joint effort.

II The author developed analysis software used to identify phases. The author also contributed to analysis of results and writing/reviewing of the manuscript.

III The author performed DFT simulations for LiF and $CsSnBr_3$. The author trained the NEP models. The author performed and analyzed the TI and optical transition calculations. The author wrote the initial draft of the manuscript, after this the writing was a joint effort.

PUBLICATIONS NOT INCLUDED IN THIS THESIS

The following publications are outside the scope of this thesis:

GPUMD 4.0: a high-performance molecular dynamics package for versatile materials simulations with machine-learned potentials
Ke Xu, Hekai Bu, Shuning Pan, Eric Lindgren, Yongchao Wu, Yong Wang, Jiahui Liu, Keke Song, Bin Xu, Yifan Li, **Tobias Hainer**, Lucas Svensson, Julia Wiktor, Rui Zhao, Hongfu Huang, Cheng Qian, Shuo Zhang, Zezhu Zeng, Bohan Zhang, Benrui Tang, Yang Xiao, Zihan Yan, Jiuyang Shi, Zhixin Liang, Junjie Wang, Ting Liang, Shuo Cao, Yanzhou Wang, Penghua Ying, Nan Xu, Chengbing Chen, Yuwen Zhang, Zherui Chen, Xin Wu, Wenwu Jiang, Esme Berger, Yanlong Li, Shunda Chen, Alexander J Gabourie, Haikuan Dong, Shiyun Xiong, Ning Wei, Yue Chen, Jianbin Xu, Feng Ding, Zhimei Sun, Tapio Ala-Nissila, Ari Harju, Jincheng Zheng, Pengfei Guan, Paul Erhart, Jian Sun, Wengen Ouyang, Yanjing Su, Zheyong Fan
Materials Genome Engineering Advances **3 (3), e70028**, 2025

Contents

List of abbreviations

CBM conduction band minimum.
CTL charge transition level.

DFT density-functional theory.

FNV Freysoldt, Neugebauer and Van de Walle.

GGA generalised gradient approximation.

LDA local density approximation.

MD molecular dynamics.
ML machine learning.
MLP machine-learned potential.
MPB morphotropic phase boundary.

NEP neuroevolution potential.

PES potential energy surface.

SNES separable natural evolution strategy.

TI thermodynamic integration.

VBM valence band maximum.

1

Introduction

The global transition toward renewable energy is one of the defining technological challenges of our time. Solar energy, in particular, holds enormous promise as an essentially limitless and clean source of power. Its widespread deployment hinges on the development of photovoltaic materials that are efficient, affordable, and stable over long operational lifetimes. While silicon-based solar cells currently dominate the market, the materials discovery landscape has been transformed over the last decade by the emergence of halide perovskites, a class of semiconductors with exceptional optoelectronic properties [1–5]. Halide perovskites have seen their power conversion efficiencies rise from a few percent to over 25% in little over a decade [6, 7], a pace of improvement unmatched in the history of photovoltaics.

Yet efficiency alone is not sufficient. For halide perovskites to fulfill their potential as a commercially viable photovoltaic technology, they must also be stable under operating conditions, that is, at elevated temperatures. It is here that a fundamental gap in our theoretical understanding becomes apparent. The properties of these materials have predominantly been studied at zero kelvin using first-principle density-functional theory (DFT) calculations. While DFT provides a rigorous and accurate framework for electronic structure calculations, its computational cost restricts both the system sizes and rate at which sampling is feasible, making the evaluation of finite-temperature properties computationally expensive. Bridging this gap between zero-kelvin theory and finite-temperature reality is a necessity for making meaningful predictions about materials under the conditions they will actually experience in a deployed device.

This limitation has only recently begun to vanish, owing to the development of machine-learned potential (MLP), models trained to reproduce DFT calculations at a fraction of the computational cost. These advances have opened the door to a new generation of finite-temperature studies that were simply not possible a few years ago.

The work presented in this thesis draws on these developments to study phase be-

havior and defect thermodynamics of semiconductors at finite temperature. One of its central contributions is in showcasing how MLP models can decipher the phase diagram and dynamics of complex perovskites, as presented in PAPER I and PAPER II. Also, we further develop and apply a computational framework for modeling point defects at finite temperature, combining MLPs with thermodynamic integration (TI) to evaluate defect formation free energies and charge transition levels (CTLs) as a function of temperature. This framework is applied in PAPER III to charged vacancies in a set of semiconductors, revealing that temperature can substantially shift charge transition levels, with direct implications for carrier concentrations, recombination dynamics and ultimately device performance.

Together, these contributions advance the broader goal of developing predictive, temperature-aware models of technologically relevant materials, a necessary step toward the rational design of stable and efficient next-generation solar cells.

1.1 Thesis outline

Chapter 2 gives an overview of the perovskite crystal structure, its structural phases and the role of phonon modes in driving phase transitions between them. Mixed halide perovskites are then introduced as a strategy for compositional engineering of photovoltaic materials with improved stability. The chapter concludes by discussing the specific compounds $MAPbI_3$, $FAPbI_3$ and $MA_{1-x}FA_xPbI_3$, and by placing the contributions of this thesis within the context of understanding their phase behavior through atomistic simulations.

Chapter 3 introduces the concept of point defects and establishes the formation free energy as the central quantity in their thermodynamic description. The CTL is derived from this free energy and is discussed both as an important factor in a material's electronic properties and as an experimentally accessible quantity against which simulations can be benchmarked. The chapter concludes by outlining the contributions of this thesis to understanding how CTLs evolve with temperature.

Chapter 4 details the computational framework employed throughout the thesis. Beginning from Schrödinger's equation, the derivation of DFT is presented as the quantum mechanical foundation underlying all calculations. MLP models are then introduced as a means of extending the accessible length and time scales while retaining DFT-level accuracy, with particular focus on the neuroevolution potential (NEP) framework used in all papers included in this thesis. The chapter concludes by describing how these potentials are applied: first within molecular dynamics (MD) simulations to sample finite-temperature configurations, and subsequently within the TI framework to evaluate free energies.

A summary of all papers included in the thesis is given in Chapter 5.

Finally, Chapter 6 offers a brief outlook on directions for future work.

2

Perovskites

Perovskites are a class of materials with the crystal structure ABX_3. The ideal cubic structure of a perovskite is illustrated in Fig. 2.1. Both the A and B site components are positively charged, while the X site atom is negatively charged. Charge neutrality requires that the combined positive charge of the A and B sites balances the negative charge of the X sites.

Halide perovskites, that is, perovskites with X site components from the halide family of atoms, have received considerable attention in recent years for their promising photovoltaic properties. Advances in halide perovskite-based semiconductors highlight their potential for use in light-emitting diodes, lasers, and solar cells [8–11]. Specifically, these materials exhibit long carrier lifetimes and strong defect tolerance, which makes them well suited for use in the photoactive layer of a solar cell [1–5]. Recently, the efficiency of perovskite-based solar cells has exceeded 25% [6, 7], rivaling that of state-of-the-art silicon-based cells.

2.1 Phases, phase transitions and phonons in perovskites

Perovskites exhibit a rich variety of structural phases, arising from the tilting and rotation of the BX_6 octahedra that form the backbone of the ABX_3 structure, seen in Fig. 2.1. At high temperatures, perovskites typically adopt a highly symmetric cubic phase. It should be noted, however, that this phase is only cubic on average, with local structures fluctuating around cubic symmetry [12]. This is of importance when modeling cubic perovskites, as sampling these fluctuations is necessary to capture their behavior. As temperature is lowered, perovskites usually go through phase transitions toward lower-symmetry phases, such as tetragonal, orthorhombic or rhombohedral

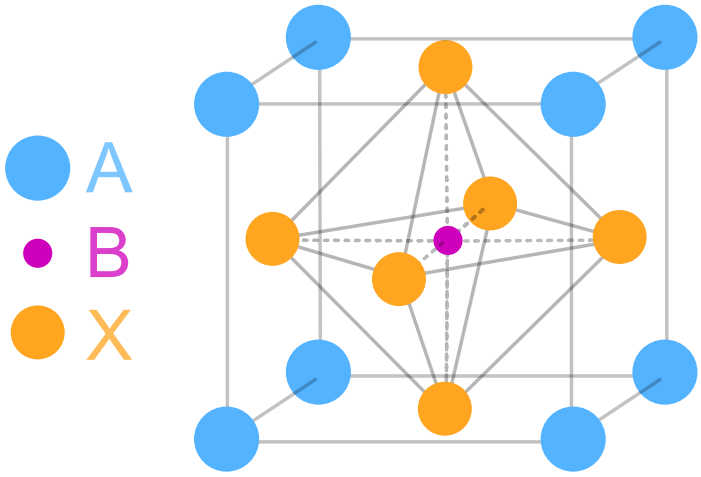

Figure 2.1: Schematic representation of the ideal cubic ABX_3 perovskite structure. The B cation is surrounded by six X anions, forming a BX_6 octahedron. The collective behavior of these octahedra is fundamental to the properties of perovskites.

phases. These phase transitions are driven by the softening of specific phonon modes, which are quantized collective vibrations of atoms in a crystal lattice. A soft mode refers to such a vibration whose restoring force vanishes as the system approaches a structural instability, leading to a transition into a structure with lower energy. Two common phonon modes responsible for this symmetry lowering are the M- and R-modes, illustrated in Fig. 2.2, representing the in-phase and out-of-phase rotations of the BX_6 octahedra, respectively. In-phase tilting is when adjacent octahedra along the rotation axis rotate in the same direction, while out-of-phase tilting corresponds to adjacent octahedra tilting in opposite directions.

Soft modes manifest as imaginary (negative) frequencies in the phonon dispersion. The phonon dispersion of the halide perovskite methylammonium lead iodide ($MAPbI_3$) is shown in Fig. 2.3, where negative frequencies are present at both the M- and R-points. This indicates that the system lowers its energy upon distorting along these modes, and will therefore adopt such a distorted configuration when not prevented from doing so by entropic effects. Despite the presence of soft modes, $MAPbI_3$ adopts a cubic phase at high temperature. This is due to the structuring being dynamically stabilized by thermal fluctuations even though lower-energy structures exist at zero kelvin.

To systematically describe the resulting distorted structures, the Glazer notation is widely employed [13]. This notation characterizes the tilting pattern using a three-letter descriptor, such as $a^+b^-c^0$. The letters a, b, and c represent the relative magnitude of the tilt about the x, y, and z axes, respectively. The superscripts indicate the phase relationship between consecutive layers of octahedra: a plus sign (+) denotes in-phase

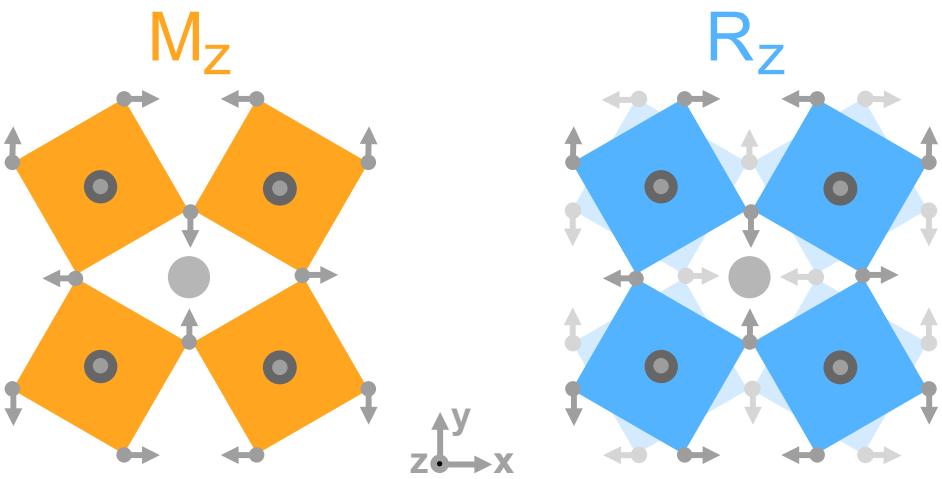

Figure 2.2: Illustration of octahedral tilt with either the M or R mode active. Note that these distortions can take place along the x, y or z-axis, with tilt along the z-axis being illustrated here.

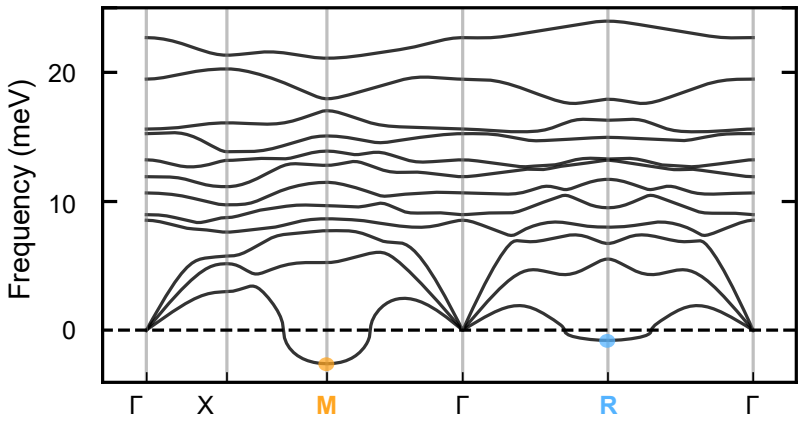

Figure 2.3: Phonon dispersion of $MAPbI_3$ in its cubic phase. Negative frequencies are present around the M and R points, highlighted with dots, indicating structural instabilities.

rotation (associated with M-modes), a minus sign (−) denotes out-of-phase rotation (associated with R-modes), and a zero (0) indicates no tilting about that specific axis. For instance, in the cubic phase the Glazer notation would read $a^0a^0a^0$ as we have no tilt around any axis. An example of an orthorhombic phase is $a^-a^-c^+$, exhibited by some perovskites at low temperatures [14], which describes out-of-phase tilting along directions x and y, and in-phase tilting along z.

A central challenge in perovskite-based photovoltaic devices is their structural stabil-

ity. Many perovskites undergo transitions to lower-symmetry phases over time, which can limit long-term device performance, while others are highly sensitive to external conditions such as temperature and pressure, leading to phase transitions and degradation. Consequently, a detailed understanding of the perovskite phase landscape is essential.

2.2 Mixed halide perovskites

In the light of stabilizing halide perovskites, mixing different compounds to create new halide perovskites has emerged as a promising strategy. The hope is to identify compositions that retain photovoltaic properties while increasing stability in comparison to the independent compositions.

A common approach is to mix halide species on the X site, to form compounds of the type $ABX_{3-x}X'_x$, where the ratio of the two halides can be tuned. Beyond halide mixing, substitution at the A and B sites has been extensively investigated to precisely tune structural and electronic properties [15]. Various A-site cations have been integrated to form mixed-cation compounds, including Cs, methylammonium (MA, CH_3NH_3), formamidinium (FA, $CH(NH_2)_2$), and guanidinium (GA, $C(NH_2)_3$). Examples of these mixtures include $MA_{1-x}FA_xPbI_3$, $MA_{1-x}FA_xPbBr_3$, $MA_{1-x}Cs_xPbI_3$, $FA_{1-x}Cs_xPbI_3$ and so on. The phase diagrams of these multi-component systems have been investigated experimentally for specific cases.

However, a comprehensive mapping of the phase diagrams of these mixtures remains challenging. The vast compositional landscape, coupled with the presence of metastable phases, makes these materials difficult to probe by experimental means alone. Consequently, a clear structural picture is often difficult to obtain. Computational approaches, including density-functional theory (DFT) and machine-learned potential (MLP) models discussed in Chapter 4, can bridge this gap by enabling simulations that clarify the behavior of these complex systems. This motivated the work presented in **PAPER I**, where a MLP model was employed to systematically explore the phase behavior of the mixed halide perovskite $MA_{1-x}FA_xPbI_3$.

2.3 Properties of $MAPbI_3$, $FAPbI_3$ and $MA_{1-x}FA_xPbI_3$

$MAPbI_3$ and formamidinium lead iodide ($FAPbI_3$) are among the most extensively studied halide perovskites, and serve as the endpoint compositions of the mixed halide perovskite $MA_{1-x}FA_xPbI_3$. The phase diagram of $MA_{1-x}FA_xPbI_3$ is investigated in **PAPER I** and the various phases and cation dynamics in $FAPbI_3$ is investigated in **PAPER II**.

$MAPbI_3$

$MAPbI_3$ has attracted significant attention due to its ease of fabrication, high power conversion efficiency and a suitable band gap for photovoltaic applications [16–20].

$MAPbI_3$ undergoes a well-established sequence of phase transitions as a function of temperature. At high temperatures it adopts the cubic ($a^0a^0a^0$) phase, transitioning on cooling first to a tetragonal phase with out-of-phase octahedral tilting ($a^0a^0c^-$), and subsequently to an orthorhombic phase ($a^-a^-c^+$) at low temperatures [14, 21, 22]. Despite its benchmark status, $MAPbI_3$ suffers from limited thermal stability, leading to it degrading over time [23].

$FAPbI_3$

$FAPbI_3$ has attracted particular interest due to its band gap and greater resistance to thermal decomposition relative to $MAPbI_3$ [24, 25]. However, its stability still remains challenging, as it with time transitions into a non-perovskite phase, not suitable for photovoltaic applications [26, 27].

At room temperature $FAPbI_3$ adopts a cubic phase ($a^0a^0a^0$), transitioning on cooling to a tetragonal phase with in-phase octahedral tilting ($a^0a^0c^+$) [28–30]. This is in contrast to the out-of-phase tilting observed in tetragonal $MAPbI_3$. The low-temperature phase of $FAPbI_3$, designated the γ-phase, remains poorly understood. Experimental studies have identified ambiguity regarding its crystal structure, with evidence for both structural disorder and competing low-energy configurations [28–31]. In **PAPER II**, large-scale molecular dynamics (MD) simulations and a systematic ground state search using a MLP model, based on the neuroevolution potential (NEP) formalism, were employed to investigate the microscopic structure of this phase. The simulations revealed that the true ground state adopts an $a^-b^-b^-$ tilt pattern, but that the system becomes kinetically trapped in a metastable $a^-a^-c^+$ configuration upon cooling, mirroring experimental observations of glassy disorder in the low-temperature phase. This is most likely the case due to a combination of the behavior of the octahedral tilt and disorder of the organic FA molecules. For the octahedra, transitioning from the tetragonal tilt pattern $a^0a^0c^+$ to the orthorhombic phase $a^-b^-b^-$ is associated with a large energy barrier, given that the transition is first order. This large energy barrier stems from all the in-phase tilts along one of the axes in $a^0a^0c^+$ having to switch to out-of-phase tilt in $a^-b^-b^-$ for the transition to occur. Furthermore, the $a^-b^-b^-$ ground state is characterized by orientational order among the organic FA cations. In practice, however, such highly ordered configurations may be difficult to achieve due to kinetic trapping at low temperatures, which leads to a glass-like structure. As the temperature decreases, the reduced mobility prevents the molecules from aligning into the specific long-range order required by the $a^-b^-b^-$ ground state. Comparisons between simulated and experimental inelastic neutron scattering spectra in **Paper II** suggest that this disorder is

also the case in practice. As shown in Fig. 2.4, the spectra obtained from the cooled structure, where the molecules exhibit disorder, show significantly better agreement with experimental data than the structures identified through the ground state search. This suggests that the orientational glass behavior acts as a secondary barrier, preventing the system from relaxing into the $a^-b^-b^-$ ground state and causing it to remain in a metastable $a^-a^-c^+$ phase.

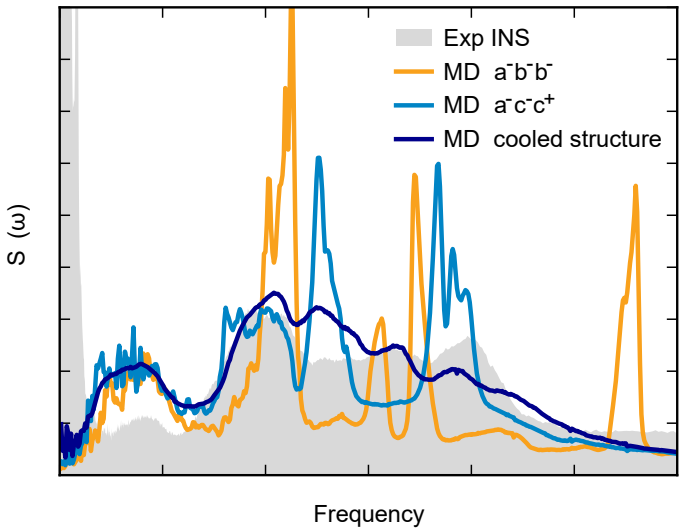

Figure 2.4: Simulated inelastic neutron scattering spectra, $S(\omega)$, are presented in comparison with experimental data obtained from Ref. [32]. The structures designated as $a^-b^-b^-$ and $a^-a^-c^+$ were generated from low-temperature MD simulations, initialized from their respective global minima identified during the ground-state search. The data labeled as "cooled structure" represents the configuration reached by cooling the system from the high-symmetry cubic phase. This cooled structure exhibits closer agreement with the experimental spectra compared to the ground-state configurations, suggesting that the experimentally observed phase corresponds to this metastable state. Both experimental and simulated spectra are scaled with an arbitrary constant to make them appear on the same scale.

$MA_{1-x}FA_xPbI_3$

Mixing MA and FA on the A-site to form $MA_{1-x}FA_xPbI_3$ has emerged as a strategy to combine the desirable properties of both endpoint compositions [33]. However, the opposing tilt patterns of the room-temperature tetragonal phases of $MAPbI_3$ ($a^0a^0c^-$) and $FAPbI_3$ ($a^0a^0c^+$) imply the existence of at least one morphotropic phase boundary (MPB) in the composition-temperature phase diagram, that is, a boundary across which the structural symmetry changes with composition. MPBs are well known in oxide

perovskites such as $PbZr_xTi_{1-x}O_3$, where they give rise to enhanced piezoelectric and dielectric properties through the near-degeneracy of competing phases [34, 35].

The phase diagram of $MA_{1-x}FA_xPbI_3$ has been probed experimentally, but no consensus could be reached [14, 15, 21, 36, 37]. In **PAPER I**, the phase diagram of $MA_{1-x}FA_xPbI_3$ was systematically mapped using MD simulations based on a MLP model. The results can be seen in Fig. 2.5a, where several experimental studies are also included. Key

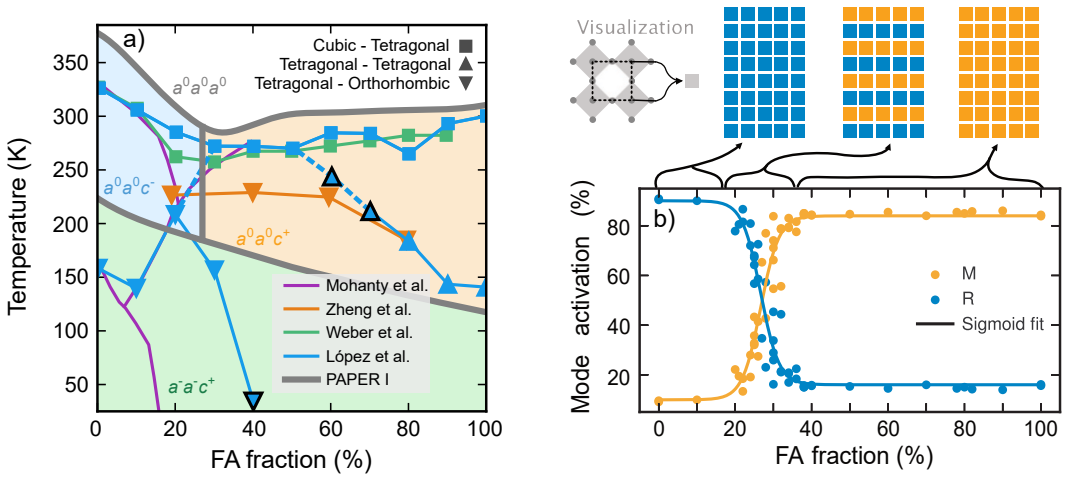

Figure 2.5: (a) Simulated phase diagram based on the results from **PAPER I** along with four experimental studies. Weber et al. [36] predicted the transition between the cubic and tetragonal phases across the entire composition. Mohanty et al. [14] studied transitions for low FA concentration structures. López et al. [21] predict similar results to Mohanty et al., but extends the composition range to include all compositions all the way to $FAPbI_3$. Zheng et al. [37] predict a transition between tetragonal and orthorhombic phases. Points outlined in black correspond to measurements with a limited data basis. (b) Phonon mode activation as a function of composition at 250 K. Illustration shows how layers of alternating octahedra tilt form.

features from the experimental studies are captured in the simulated phase diagram, such as the transition between cubic and tetragonal for the entire composition range and the two transitions at both low and high FA concentration. The identification was particularly difficult in the intermediate composition range, where the results of experimental studies diverged. Here, our simulations identified a MPB, which is a phase transition driven by a change in composition, appearing around 27% FA between the phases $a^0a^0c^-$ and $a^0a^0c^+$. Near this boundary, the free energy landscapes of the M- and R-point phonon modes become nearly degenerate, giving rise to nanoscale layered structures with alternating tilt patterns and suggesting minimal interface energy between the competing phases. This is illustrated in Fig. 2.5b, which shows the active phonon modes as a function of composition at 250 K. At low FA concentration the R-mode is active and at high FA concentration the M-mode is active. Between these,

there is a continuous crossover between these modes, with them being equally present in the system at the MPB. This smooth crossover between the modes is mediated by the formation of layers of either M- or R-modes, with the FA concentration determining the distribution of layers. This is illustrated in Fig. 2.5b, where the tilt mode of each unit cell transitions from uniformly R-dominated at low FA content, through a mixed intermediate region at the MPB, to uniformly M-dominated at high FA content. The formation of nanoscale layers with alternating tilt patterns makes the assignment of a single crystal structure to a macroscopic sample increasingly difficult, providing a natural explanation for the lack of experimental consensus for the phases of $MA_{1-x}FA_xPbI_3$.

Furthermore, band edge fluctuations are found to peak near the MPB, indicating enhanced electron-phonon coupling with direct implications for charge transport and optoelectronic performance. This result is based on DFT calculations of MD snapshots simulated at 330 K, a temperature at which the majority of the compositions is in a cubic phase and no MPB is to be found. The reason why we still see a peak in the band edge fluctuations around the MPB is most likely that the similar free energy landscape of the M- and R-modes at the MPB also extends to higher temperatures. Enhanced electron-phonon coupling have been measured in previous experiments, the results of which is in agreement with the band edge fluctuation observed here [21].

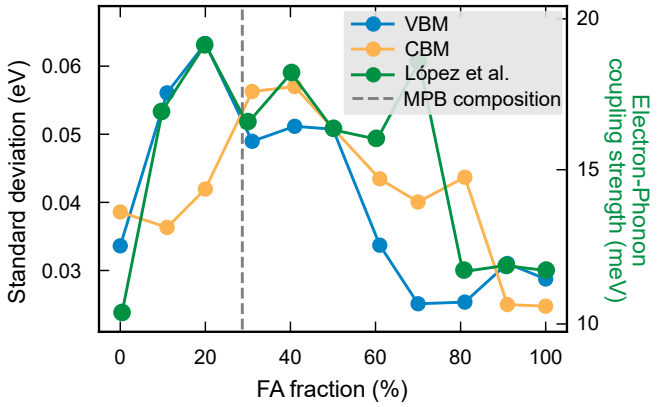

Figure 2.6: Standard deviations of the valence band maximum (VBM) and conduction band minimum (CBM) levels as a function of FA composition at 330 K compared with electron-phonon coupling strength measurements from López et al. [21].

3

Defects

In real materials, crystal structures are rarely perfectly ordered and commonly exhibit defects such as grain boundaries and dislocations [38]. Among these, point defects form a fundamental class, including vacancies, interstitials, and substitutional defects. A vacancy occurs when an atom is missing from its regular lattice site, an interstitial defect arises when an atom occupies a position between normal lattice sites, and a substitutional defect is formed when a host atom is replaced by a different atomic species. How different point defects can look like is illustrated in Fig. 3.1. When a defect is introduced into a insulator or semiconductor, it introduces new energy levels within the band gap, states that would not exist in a perfect crystal. These levels are classified as either shallow or deep depending on their position within the band gap [39, 40]. Shallow defects introduce levels close to the band edges, near the valence band maximum (VBM) or conduction band minimum (CBM), and the associated charge is spread diffusely across the material. Deep defects, on the other hand, introduce levels further from the band edges, closer to the middle of the band gap. Here, the charge is tightly localized around the defect site, which can significantly disturb the surrounding atomic lattice and strongly influence the electronic, optical, and mechanical properties of the material. Since defects influence material properties, they can be turned from an imperfection into a tool, deliberately introduced and controlled through defect engineering to tailor material properties for specific applications, with doping in semiconductors being a prime example.

Experimentally, techniques to probe defects are notoriously difficult. These techniques probe different physical signatures of defects: electron paramagnetic resonance is sensitive to unpaired electron spins, scanning tunneling spectroscopy detects the local electronic structure of defects near surfaces, deep-level transient spectroscopy probes charged defect states in semiconductors and positron annihilation spectroscopy is particularly sensitive to open-volume defects such as vacancies [39, 41–45]. Com-

putational modeling also plays an essential role in the understanding of point defects, providing an atomic-scale insight. This can aid to interpret experimental observations and bridge the gap between measured signals and the underlying physics.

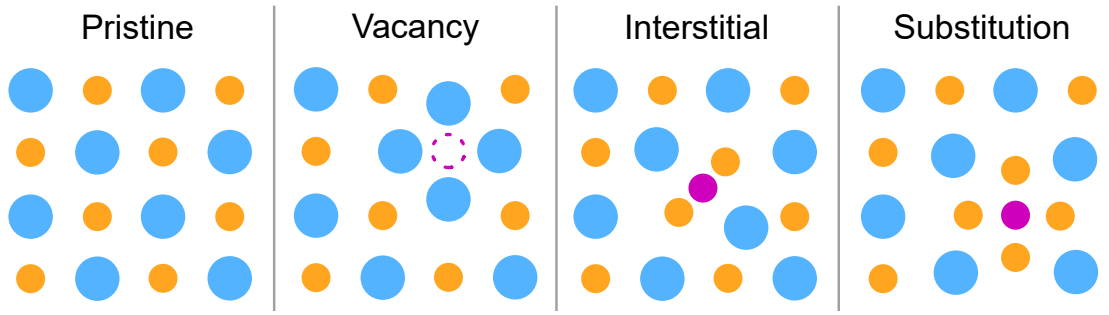

Figure 3.1: Illustration of pristine and defective structures. For the defective structures, note that the local environment around each atom is slightly distorted.

3.1 Thermodynamics of defects

The central quantity in modeling defect properties is the formation free energy [39], as it provides direct insight into several key characteristics, including the stability and concentration of defects. The formation free energy is defined as the free energy cost of introducing a defect into an otherwise perfect crystal and depends on external conditions such as temperature, pressure and the chemical potential of the atomic species being exchanged with a reservoir. Historically, defect properties have predominantly been investigated at zero kelvin, as the configurational sampling required at finite temperature is computationally infeasible with density-functional theory (DFT), which has been the main method to obtain these energies. Recent developments in machine learning (ML) methods have made sampling considerably more efficient, enabling larger systems to be studied over longer timescales. This has opened the door to studying the finite-temperature behavior of defects. Due to these advances, obtaining the properties of defects at finite temperatures is now possible.

The formation free energy of a point defect X with charge state q is defined as [39],

$$G^f[X^q] = G_{\text{tot}}[X^q] - G_{\text{tot}}[\text{bulk}] - \sum_i n_i \mu_i + q(E_{\text{VBM}} + \mu_e) + E_{\text{corr}}. \tag{3.1}$$

Here, $G_{\text{tot}}[X^q]$ and $G_{\text{tot}}[\text{bulk}]$ is the Gibbs free energy for the defect-containing and pristine systems, respectively. $\sum_i n_i \mu_i$ is the chemical potential contribution to the Gibbs free energy when removing ($n_i < 0$) or adding ($n_i > 0$) a defect. The term $q(E_{\text{VBM}} + \mu_e)$ accounts for the energy required to add or remove q electrons, where

E_{VBM} is the VBM position and μ_e is the electron chemical potential, also called Fermi-level, in reference to the VBM. Finally, E_{corr} is the correction energy for finite-size effects, particularly important for charged defects due to long-range Coulomb interactions in periodic supercells [46, 47]. An illustration of defect formation energy can be seen in Fig. 3.2, which shows three different charge states as a function of Fermi-level. While the formation free energy is the standard tool in defect modeling, it is not itself an experimental observable. Rather, it serves as the basis for deriving quantities that are.

One such quantity is the defect concentration. Since the formation energy represents the work required to create a defect, it directly governs how favorable defect formation is, and the equilibrium concentration c follows as,

$$c = N \exp\left(-\frac{G^f[X^q]}{k_B T}\right), \tag{3.2}$$

where N is the number of available sites, k_B is Boltzmann's constant, and T is the temperature.

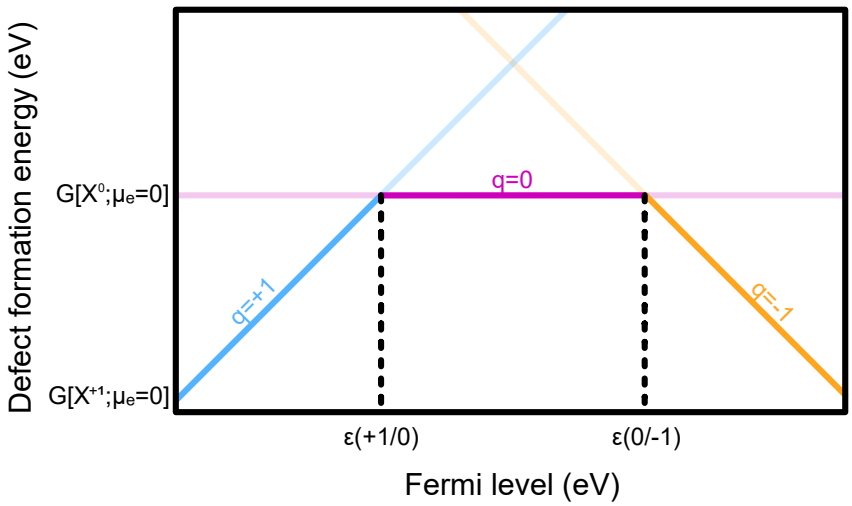

Figure 3.2: Illustration of charge transition levels for a defect with three charge states, $q = -1, 0, 1$. The slope of each formation free energy line is determined solely by the charge state q, while the positions of the charge transition levels (CTLs) are obtained from the formation free energies evaluated at the VBM together with the corresponding charge values, as in Eq. (3.3).

Another such quantity is the CTL, or thermodynamic transition level, which describes localized electronic states that defects can introduce into the band gap [39]. The

CTL is defined as the Fermi-level at which two charge states have equal formation free energy, marking the point where the preferred charge state changes. As CTLs are additional levels within the band gap they define accessible electronic states that can trap or release carriers, affecting carrier concentrations, recombination dynamics, and charge transport. Accurate determination of CTLs is therefore critical for understanding and predicting the electronic behavior of defective semiconductors and insulators.

A CTL, denoted $\varepsilon(q_1/q_2)$, represents the Fermi-level where the most stable charge state of a defect changes from q_1 to q_2 based on their formation free energy, defined as,

$$\epsilon(q_1/q_2) = \frac{G^f[X^{q_1}; \mu_e = 0] - G^f[X^{q_2}; \mu_e = 0]}{q_2 - q_1}. \tag{3.3}$$

When plotting defect formation energy against the Fermi-level, each charge state appears as a line with slope q, and the CTLs are given by the intersection of these. This is illustrated in Fig. 3.2, where the points at which the charge state with the lowest free energy changes defines a CTL, marked with vertical dashed lines.

3.2 The effect of temperature on charged vacancies

CTLs can be observed experimentally, providing valuable insight into the properties of a semiconductor. Furthermore, they provide grounds on which we can compare our simulations with experiments. Previously, first-principles DFT studies have been the main basis of such comparisons. While DFT provides a rigorous framework for modeling defects, its computational cost limits system sizes and sampling frequency, making the evaluation of temperature-dependent effects computationally challenging. The temperature dependence of CTLs is primarily governed by vibrational entropy, which is the dominant entropic contribution to the formation free energy [48]. Other sources of entropy, such as spin, electronic and orientational contributions, are secondary effects that are generally assumed to have a negligible influence in comparison. Accurately capturing vibrational entropy requires finite-temperature sampling, which is computationally infeasible using DFT alone. However, over the last few years machine-learned potential (MLP) models have gained traction as an alternative for modeling point defects [48–50]. This has enabled accurate and fast sampling, unlocking the ability to predict the temperature dependence of CTLs and other defect-related properties.

In **PAPER III**, the temperature dependence of vacancy CTLs was investigated across several semiconductors using the methods outlined in Chapter 4. The systems considered were MgO, LiF, and $CsSnBr_3$, focusing on O, F, and Br vacancies, respectively. The charge states considered were 0 and +2 for O in MgO, while −1, 0, and +1 were evaluated for LiF and $CsSnBr_3$. Both the vibrational entropy contributions and the

temperature-induced VBM shifts were explicitly accounted for in order to track the thermal evolution of the CTLs. By accounting for these thermal effects, we find that the CTLs are not static, with those in MgO and LiF shifting by hundreds of meV between zero kelvin and room temperature, see Fig. 3.3a, b. For the Br vacancy in $CsSnBr_3$, we find a smaller overall shift of the CTLs, see Fig. 3.3c. However, an entirely new charge state emerges as stable around 60 K, not present in the zero-kelvin picture. This means that even modest shifts in CTL energy can qualitatively alter the predictions.

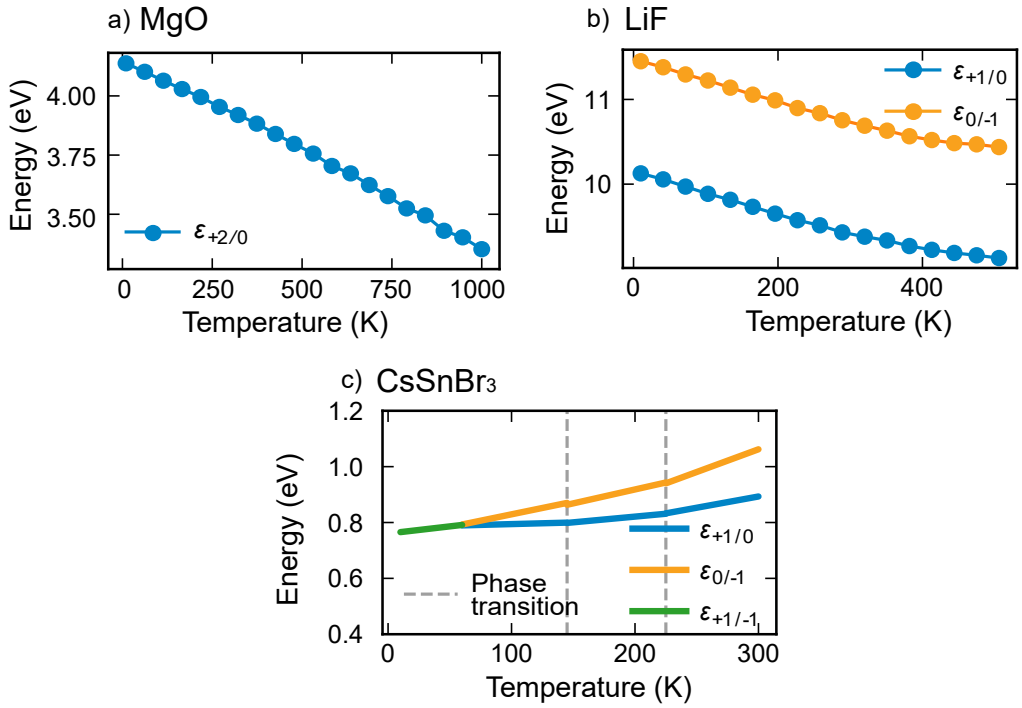

Figure 3.3: CTLs for vacancies in MgO, LiF, and $CsSnBr_3$ as a function of temperature, referenced to the VBM. For MgO and LiF, the CTLs shift by several hundred meV across the temperature range, reflecting the influence of vibrational entropy and changes in the VBM. $CsSnBr_3$ exhibits smaller overall shifts. However, around 60 K, the neutral charge state becomes stable, an effect not captured in the zero-kelvin picture.

Experiments have indicated that CTLs can shift with temperature. Redkin et al. [51] probed Ga vacancies in GaSe, showing that the CTLs $\varepsilon_{0/-1}$ and $\varepsilon_{-1/-2}$ both shift with temperature. A relative shift between these two levels is also observed, indicating that the effect cannot be attributed solely to VBM movement. The magnitude of the total shift over the temperature range studied by Redkin et al. also agrees with our results.

Overall, the findings in **PAPER III** demonstrate that the traditional zero-kelvin approach can lead to qualitatively incorrect predictions of CTL positions, and that explicitly accounting for vibrational entropy and VBM shifts is necessary for an accurate description.

4

Computational modeling

This chapter summarizes the computational methods used throughout the thesis. It begins with density-functional theory (DFT), which provides the reference energies and forces forming the basis for all subsequent calculations. DFT data is used to train machine-learned potential (MLP) models within the neuroevolution potential (NEP) formalism, extending simulations to larger length and time scales. The MLP is then applied in molecular dynamics (MD) simulations to sample finite-temperature properties. The chapter concludes with thermodynamic integration (TI), through which free energies of defects are accurately determined.

4.1 Schrödinger's equation and density functional theory

All properties of an atomic structure is described by the wave function of the system, obtained by solving the time-independent Schrödinger equation [52],

$$\hat{H}\Phi = E_{\text{tot}}\Phi \tag{4.1}$$

where $\hat{H}$ is the Hamiltonian and E_{tot} is the total energy of the system. The many-body wave function $\Phi = \Phi(\mathbf{r}_1, \mathbf{r}_2, \ldots, \mathbf{R}_1, \mathbf{R}_2, \ldots)$ depends on the positions of all electrons $\{\mathbf{r}_i\}$ and ions $\{\mathbf{R}_n\}$. For a crystal containing electrons and ions, the full Hamiltonian is,

$$\begin{aligned}\hat{H} = &\underbrace{-\sum_n \frac{\hbar^2}{2M_n}\nabla_n^2}_{\hat{T}_\mathrm{R}} + \underbrace{\frac{1}{4\pi\varepsilon_0}\frac{1}{2}\sum_{n\neq m}\frac{Z_n Z_m e^2}{|\mathbf{R}_n - \mathbf{R}_m|}}_{\hat{V}_\mathrm{R}} - \underbrace{\sum_i \frac{\hbar^2}{2m_e}\nabla_i^2}_{\hat{T}_\mathrm{r}} \\ &+ \underbrace{\frac{1}{4\pi\varepsilon_0}\frac{1}{2}\sum_{i\neq j}\frac{e^2}{|\mathbf{r}_i - \mathbf{r}_j|}}_{\hat{V}_\mathrm{r}} - \underbrace{\frac{1}{4\pi\varepsilon_0}\sum_{i,n}\frac{Z_n e^2}{|\mathbf{r}_i - \mathbf{R}_n|}}_{\hat{V}_\mathrm{r,R}} \\ = &\underbrace{\hat{T}_\mathrm{R} + \hat{V}_\mathrm{R}}_{\text{Ionic}} + \underbrace{\hat{T}_\mathrm{r} + \hat{V}_\mathrm{r}}_{\text{Electronic}} + \underbrace{\hat{V}_\mathrm{r,R}}_{\text{Electron-ion}} .\end{aligned} \tag{4.2}$$

The five terms describe all types of interactions in the crystal considered in this thesis:

- $\hat{T}_\mathrm{R}$: **ionic kinetic energy** — the kinetic energy of each ion
- $\hat{V}_\mathrm{R}$: **ion–ion repulsion** — the Coulomb repulsion between pairs of ions
- $\hat{T}_\mathrm{r}$: **electronic kinetic energy** — the kinetic energy of each electron
- $\hat{V}_\mathrm{r}$: **electron–electron repulsion** — the Coulomb repulsion between pairs of electrons
- $\hat{V}_\mathrm{r,R}$: **electron–ion attraction** — the Coulomb attraction between electrons and ions

Solving solving the many-body Schrödinger equation analytically is not feasible for almost all systems of practical interest, approximations are therefore necessary.

One simplification arises from the large mass difference between ions and electrons. Because ions are several orders of magnitude heavier than electrons, they move on a much slower timescale, and can therefore be treated as stationary from the perspective of the electrons. This allows us to neglect the ionic kinetic energy $\hat{T}_\mathrm{R}$ in the electronic Hamiltonian and, since the ions are fixed, to treat the ion–ion repulsion $\hat{V}_\mathrm{R}$ as a constant for a given ionic configuration. This is the Born–Oppenheimer approximation [53], which reduces the problem to solving a purely electronic Schrödinger equation,

$$\hat{H}_e\Phi_e = \left[\hat{T}_\mathrm{r} + \hat{V}_\mathrm{r} + \hat{V}_\mathrm{r,R}\right]\Phi_e = E\Phi_e. \tag{4.3}$$

Here the ionic positions $\{\mathbf{R}_n\}$ enter only as fixed parameters rather than dynamical variables. The electronic ground-state energy $E(\{\mathbf{R}_n\})$ forms one part of the effective

potential energy surface (PES) governing the ionic motion, the other being the ion-ion interaction $\hat{V}_{\mathrm{R}}$ [54]. The nuclear Schrödinger equation can thus be written as

$$\left[\hat{T}_{\mathrm{R}} + \hat{V}_{\mathrm{R}} + E(\mathbf{R}_1, \ldots, \mathbf{R}_M)\right] \chi = E_{\mathrm{tot}} \chi. \tag{4.4}$$

Obtaining this PES is the central goal, as it provides the foundation for evaluating the dynamics and properties of a crystal structure. However, solving for this energy exactly still remains computationally unfeasible for all but the smallest systems. At this point, DFT offers a route forward by formulating the many-body electronic problem in terms of the ground-state electron density of an auxiliary system of non-interacting particles.

4.1.1 The Hohenberg-Kohn theorems and Kohn-Sham equations

DFT is grounded in the Hohenberg-Kohn theorems [55] and made computationally practical through the Kohn-Sham equations [56]. The first Hohenberg-Kohn theorem states that the external potential $V_{\mathrm{ext}}(\mathbf{r})$, typically the static Coulomb potential created by the nuclei, is uniquely determined by the ground-state electron density $\rho(\mathbf{r})$, and vice versa. The ground-state density is defined as the probability of finding any one electron at position $\mathbf{r}$, obtained by integrating the many-body probability density over all other electron coordinates,

$$\rho(\mathbf{r}) = N \int \cdots \int |\Psi(\mathbf{r}, \mathbf{r}_2, \ldots, \mathbf{r}_N)|^2 \, \mathrm{d}\mathbf{r}_2 \cdots \mathrm{d}\mathbf{r}_N.$$

This implies that all ground-state properties of the system are functionals of $\rho(\mathbf{r})$ alone, reducing the problem from a $3N$-dimensional wave function to a function of just three spatial coordinates.

The second Hohenberg-Kohn theorem states that the total energy can be written as a functional of the electron density, $E[\rho(\mathbf{r})]$, and that this functional is minimized by the exact ground-state density $\rho_0(\mathbf{r})$. This gives a variational route to the ground-state energy without ever solving the full many-body Schrödinger equation. The energy functional takes the form,

$$E[\rho] = T[\rho] + \int V_{\mathrm{ext}}(\mathbf{r}) \, \rho(\mathbf{r}) \, \mathrm{d}\mathbf{r} + E_{\text{e-e}}[\rho], \tag{4.5}$$

where $T[\rho]$ is the kinetic energy of the electrons, $\int V_{\mathrm{ext}}(\mathbf{r})\rho(\mathbf{r}) \, \mathrm{d}\mathbf{r}$ is the energy due to the external potential, and $E_{\text{e-e}}[\rho]$ is the electron–electron interaction energy. Finding the density ρ_0 that minimizes Eq. (4.5) thus directly yields the ground-state energy.

While the Hohenberg-Kohn theorems are exact, they offer no practical path for computing Eq. (4.5) without knowledge of the many-body wave function. The Kohn-Sham ansatz addresses this by replacing the interacting system with an auxiliary system of

non-interacting particles that, by construction, reproduces the exact ground-state density. All many-body effects that are omitted by this substitution are absorbed into a single exchange-correlation functional $E_{\mathrm{xc}}[\rho]$. The electron density is constructed from a set of single-particle Kohn-Sham orbitals $\{\phi_i\}$ as $\rho(\mathbf{r}) = \sum_i |\phi_i(\mathbf{r})|^2$, and the total energy takes the form,

$$E[\rho] = T^{\mathrm{KS}}[\rho] + \int V_{\mathrm{ext}}(\mathbf{r})\,\rho(\mathbf{r})\,\mathrm{d}\mathbf{r} + E_H[\rho] + E_{\mathrm{xc}}[\rho], \tag{4.6}$$

where $T^{\mathrm{KS}}[\rho]$ is the kinetic energy of the non-interacting system, $E_H[\rho]$ is the Hartree energy capturing the classical electron-electron repulsion, and $E_{\mathrm{xc}}[\rho]$ corrects for the error introduced by replacing the true interacting kinetic energy and many-body interactions with their non-interacting counterparts. This exchange-correlation can therefore simply be expressed as the difference between Eq. (4.5) and Eq. (4.6),

$$E_{\mathrm{xc}}[\rho] = \underbrace{T[\rho] - T^{\mathrm{KS}}[\rho]}_{\text{Kinetic error}} + \underbrace{E_{\text{e-e}}[\rho] - E_H[\rho]}_{\text{Potential error}}.$$

Various ways of estimating the exchange-correlation term are discussed in Sect. 4.1.2.

Minimizing the energy functional $E[\rho]$ with respect to the single-particle orbitals $\{\phi_i\}$ yields the set of Kohn-Sham equations,

$$\left[-\frac{1}{2}\nabla^2 + V_{\mathrm{eff}}(\mathbf{r})\right]\phi_i(\mathbf{r}) = \varepsilon_i\phi_i(\mathbf{r}), \tag{4.7}$$

where the effective potential V_{eff} is defined as the sum of the external, Hartree, and exchange-correlation contributions,

$$V_{\mathrm{eff}}(\mathbf{r}) = V_{\mathrm{ext}}(\mathbf{r}) + V_{\mathrm{H}}(\mathbf{r}) + V_{\mathrm{xc}}(\mathbf{r}). \tag{4.8}$$

The Hartree and exchange-correlation potentials are determined via the functional derivatives of their respective energy terms with respect to the electron density $\rho(\mathbf{r})$,

$$V_{\mathrm{H}}(\mathbf{r}) = \frac{\delta E_{\mathrm{H}}[\rho]}{\delta\rho(\mathbf{r})} = \int \frac{\rho(\mathbf{r}')}{|\mathbf{r}-\mathbf{r}'|}d\mathbf{r}', \tag{4.9}$$

$$V_{\mathrm{xc}}(\mathbf{r}) = \frac{\delta E_{\mathrm{xc}}[\rho]}{\delta\rho(\mathbf{r})}. \tag{4.10}$$

Solving Eq. (4.7) yields a set of Kohn-Sham eigenvalues $\{\varepsilon_i\}$ which can be used to calculate the ground-state total energy as [56],

$$E[\rho] = \sum_i \varepsilon_i - E_{\mathrm{H}}[\rho] + E_{\mathrm{xc}}[\rho] - \int V_{\mathrm{xc}}(\mathbf{r})\rho(\mathbf{r})\,\mathrm{d}\mathbf{r}. \tag{4.11}$$

This formulation is necessary because the sum of eigenvalues overcounts the electron-electron interactions, as each ε_i already accounts for the full effective potential felt by that orbital. Specifically, the subtraction of $E_{\mathrm{H}}[\rho]$ removes the double-counted classical electrostatic repulsion, while the remaining terms, $E_{\mathrm{xc}}[\rho] - \int V_{\mathrm{xc}}(\mathbf{r})\rho(\mathbf{r})\,\mathrm{d}\mathbf{r}$, provide the necessary exchange-correlation correction. This correction arises because the exchange-correlation potential V_{xc} is the functional derivative of the energy; consequently, its integrated contribution to the eigenvalues does not generally equal the total exchange-correlation functional $E_{\mathrm{xc}}[\rho]$.

The ground-state density and total energy are obtained through the self-consistent solution of the Kohn–Sham equations. Since the effective potential depends on the density, and the density is constructed from the Kohn-Sham orbitals, the problem requires an iterative procedure.

One begins with constructing the effective potential based on the external potential $V_{\mathrm{ext}}(\mathbf{r})$ and an initial guess for the electron density $\rho^{(0)}$. With this effective potential fixed, the Kohn-Sham single-particle equations are solved to obtain a new set of orbitals $\{\phi_i\}$ and eigenvalues $\{\varepsilon_i\}$. A new density, $\rho^{(1)}$, is then formed. Using Eq. (4.11), the total energy $E[\rho^{(1)}]$ is calculated and compared to the energy from the previous iteration $E[\rho^{(0)}]$. If the difference $\Delta E = \left|E[\rho^{(1)}] - E[\rho^{(0)}]\right|$ exceeds a predefined convergence criterion, a new input density is constructed, often through a mixing scheme of the input and output densities, and the cycle is repeated. Once this criterion is met, the system is considered to have reached self-consistency, and the resulting density is identified as the physical ground-state density.

4.1.2 Exchange-correlation functionals

In practice, the exact form of $E_{\mathrm{xc}}[\rho]$ is unknown and must be approximated. The simplest approximation is the local density approximation (LDA), which assumes that the exchange-correlation energy at each point depends only on the local electron density $\rho(\mathbf{r})$, treating the system as a locally uniform electron gas. While LDA is computationally efficient, it tends to overbind molecules and underestimate lattice constants, as it neglects any information about how rapidly the density varies in space. The generalised gradient approximation (GGA) addresses this by incorporating the gradient of the density $\nabla\rho(\mathbf{r})$, making it better suited to systems with inhomogeneous charge distributions such as surfaces and molecules. Widely used GGA functionals include PBE [57] and PBEsol [58], the latter being optimized for solids and their surfaces. Hybrid functionals go further by mixing a fraction of exact Hartree-Fock exchange into the GGA exchange-correlation energy, which mitigates the self-interaction error present in pure density-based functionals and improves the description of band gaps and localized electronic states. An example is HSE06 [59]. The increased accuracy of hybrids comes at significantly greater computational cost. The choice of functional therefore represents a practical trade-off between accuracy and computational expense, and remains one of

the central approximations in any DFT calculation.

4.2 Machine-learned potentials

Although several approximations to enhance the computational efficiency of PES evaluation were discussed in the previous section, the direct application of DFT remains computationally demanding when modeling the large-scale systems or long-time dynamics necessary to capture certain finite-temperature phenomena. Therefore, we need a more efficient method to obtain the PES. In recent years, MLPs have emerged as a standard approach to this problem, providing machine learning (ML) models trained to predict energies, forces, and virials at a fraction of the computational cost of DFT. There is a large selection of these models, ranging from Gaussian processes to graph neural networks[60, 61]. Every paper included in this thesis utilizes MLP models based on the fourth generation NEP framework [62], as implemented in GPUMD[63, 64].

4.2.1 Neuroevolution potential models

A NEP model is a type of MLP that uses a feed-forward neural network to predict per-atom energies, $E_i(\mathbf{q}^i)$, with all parameters optimized using an evolutionary training scheme. These atomic energies are functions of a descriptor vector, $\mathbf{q}^i$, which encodes the local chemical environment of atom i within a cutoff radius R_c. The use of descriptor vectors ensures invariance under rotations and translations of the structure as well as permutations of atoms, symmetries that are not inherently preserved by a standard Cartesian coordinate representation [65]. The specific construction of these descriptors is detailed later in this section. The total potential energy of a system containing N atoms is obtained by summing these individual contributions, $E_{\text{tot}} = \sum_{i=1}^{N} E_i(\mathbf{q}^i)$. This defines the PES that ions experience. The energy of atom i is evaluated by a feed-forward neural network with one hidden layer,

$$E_i(\mathbf{q}^i) = \sum_{\mu=1}^{N_{\text{neu}}} w_\mu^{(1)} \tanh\left(\sum_{\nu=1}^{N_{\text{des}}} w_{\mu\nu}^{(0)} q_\nu^i - b_\mu^{(0)} \right) - b^{(1)}. \tag{4.12}$$

Here, N_{neu} is the number of neurons in the hidden layer, N_{des} is the size of the descriptor vector, $\{w\}$ are the weights for the network and $\{b\}$ are the biases.

The descriptor vector $\mathbf{q}^i$ is composed of radial and angular terms. The radial part has components q_n^i with $0 \leq n \leq n_{\text{max}}^R$,

$$q_n^i = \sum_{j \neq i} g_n(R_{ij}),$$

where R_{ij} is the distance between atoms i and j, and the sum runs over all neighboring atoms within some cutoff radius, R_c. The angular part, illustrated here with the three-body term, has components q^i_{nl} with $0 \leq n \leq n^A_{\max}$ and $1 \leq l \leq l_{\max}$,

$$q^i_{nl} = \sum_{j \neq i} \sum_{k \neq i} g_n(R_{ij})\, g_n(R_{ik})\, P_l(\cos\theta_{ijk}),$$

where θ_{ijk} is the bond angle of the triplet (i, j, k), and P_l is a Legendre polynomial. The functions $g_n(R)$ are radial functions expanded in a smooth, complete basis $\{f_k(R)\}$,

$$g_n(R_{ij}) = \sum_k c^{IJ}_{nk}\, f_k(R_{ij}).$$

The coefficients c^{IJ}_{nk} are trainable parameters that depend on the pair of chemical species (I, J) of atoms i and j. They therefore encode element-specific interactions directly in the descriptor. Because each descriptor component is constructed as a sum over all neighbors of a given species within the cutoff, it is invariant to any permutation of atoms of the same type, as the summation is independent of the ordering of neighbors. Furthermore, the neural-network parameters $\mathbf{w}^I$ (weights/biases) are also species-specific for the central atom type I, improving the perfromance of NEP models on many-component systems. For a system with two atomic species A and B, the trainable parameters of the NEP model are $\mathbf{w}^A$, $\mathbf{w}^B$, $\mathbf{c}^{AA}$, $\mathbf{c}^{BB}$, and $\mathbf{c}^{AB}$.

Forces and virials are obtained analytically from the per-atom energies via differentiation of Eq. (4.12). The force acting on atom i due to atom j is given by,

$$\mathbf{F}_{ij} = \frac{\partial E_i}{\partial R_{ij}} - \frac{\partial E_j}{\partial R_{ji}},$$

where $\partial E_i/\partial R_{ij}$ and $\partial E_j/\partial R_{ji}$ are partial forces. The total force on atom i is then,

$$\mathbf{F}_i = \sum_j \mathbf{F}_{ij}.$$

Finally, to obtain virials we evaluate,

$$\mathbf{W}_i = \sum_{j \neq i} R_{ij} \otimes \frac{\partial E_i}{\partial R_{ij}}.$$

All parameters are optimized using the separable natural evolution strategy (SNES) algorithm, which minimizes the following loss function used across all papers in this thesis,

$$
\begin{aligned}
L(\mathbf{z}) \;= \lambda_e & \left(\frac{1}{N_{\text{str}}} \sum_{n=1}^{N_{\text{str}}} \left(U^{\text{NEP}}(n, \mathbf{z}) - U^{\text{tar}}(n) \right)^2 \right)^{1/2} \\
& + \lambda_f \left(\frac{1}{3N} \sum_{i=1}^{N} \left(F_i^{\text{NEP}}(\mathbf{z}) - F_i^{\text{tar}} \right)^2 \right)^{1/2} \\
& + \lambda_v \left(\frac{1}{6N_{\text{str}}} \sum_{n=1}^{N_{\text{str}}} \sum_{\mu\nu} \left(W_{\mu\nu}^{\text{NEP}}(n, \mathbf{z}) - W_{\mu\nu}^{\text{tar}}(n) \right)^2 \right)^{1/2} \\
& + \underbrace{\lambda_1 \left(\frac{1}{N_{\text{par}}} \sum_{n=1}^{N_{\text{par}}} |z_n| \right)}_{\mathbf{L}_1} + \underbrace{\lambda_2 \left(\frac{1}{N_{\text{par}}} \sum_{n=1}^{N_{\text{par}}} z_n^2 \right)^{1/2}}_{\mathbf{L}_2} .
\end{aligned}
\tag{4.13}
$$

where λ_e, λ_f, λ_v, λ_1 and λ_2 are hyperparameters weighting the energy, force, virial, $\mathbf{L}_1$ and $\mathbf{L}_2$ terms, respectively. Superscripts NEP and tar denote the predicted and target quantities. N_{str} is the number of training structures, N the number of atoms and N_{par} is the number of trainable parameters. The $\mathbf{L}_1$ and $\mathbf{L}_2$ terms are regularization penalties that constrain the magnitude of the trainable parameters, reducing the risk of overfitting.

The SNES algorithm optimizes the trainable parameters $\mathbf{z}$ by maintaining and iteratively refining a distribution, parameterized by a mean vector $\mathbf{m}$ and standard deviation vector $\mathbf{s}$, over parameter space. We draw N_{pop} samples from this distribution, each of which is evaluated with the loss function $L(\mathbf{z_k})$, $1 \leq k \leq N_{\text{pop}}$. Samples are ranked by their loss and assigned weights accordingly, which are then used to update the distribution via the natural gradient.

4.2.2 NEP models for defective systems

How can we accurately capture the PES of a crystal structure with defects? More importantly, how can we account for the multiple charge states these defects can adopt? Here, a framework for modeling the PES of structures with deep defects is discussed, as used in **PAPER III**.

The most intuitive path to obtaining the PES of a system with a defect that can exhibit several charge states is to create one MLP model per charge state. This is best done by obtaining a set of training data for the pristine system and a set of training data per defect charge state. Each MLP is then trained on the pristine data in combination with the defect training data of its corresponding charge state. This will result in several MLP

models, that if trained well enough should be able to reproduce the PES of a defective system.

These models do however have one issue: no size-consistency. Properties, such as the charge transition level (CTL), that are computed from differences in formation free energy should be independent of the number of atoms, provided that the system is sufficiently converged. However, independent models will inevitably assign different energies to atoms far from the defect, making them fundamentally incompatible with reliable formation energy calculations. To highlight this, we write the formation free energies for defects with different charge, q and q', calculated with different models M_q and $M_{q'}$ as:

$$G^f_{M_q}[X^q] = G_{\text{tot},M_q}[X^q] - G_{\text{tot},M_q}[\text{bulk}] - \dots$$
$$G^f_{M_{q'}}[X^{q'}] = G_{\text{tot},M_{q'}}[X^{q'}] - G_{\text{tot},M_{q'}}[\text{bulk}] - \dots$$

If we are to calculate the CTL from these results, we get,

$$\begin{aligned}\epsilon(q/q') &= \frac{G^f_{M_q}[X^q] - G^f_{M_{q'}}[X^{q'}]}{q' - q} \\ &= \frac{G_{\text{tot},M_q}[X^q] - G_{\text{tot},M_q}[\text{bulk}] - G_{\text{tot},M_{q'}}[X^{q'}] + G_{\text{tot},M_{q'}}[\text{bulk}]}{q' - q} \\ &= \frac{G_{\text{tot},M_q}[X^q] - G_{\text{tot},M_{q'}}[X^{q'}] + \Delta G[\text{bulk}]}{q' - q}.\end{aligned}$$

Here, $\Delta G[\text{bulk}]$ is the difference between the pristine cells and will scale with the number of atoms in the cells as $\Delta G[\text{bulk}] = N\delta\varepsilon$, where $\delta\varepsilon$ is the energy difference between the non defective atoms in the different models. This term is in part canceled by contributions far from the defects in $G_{\text{tot},M_q}[X^q] - G_{\text{tot},M_{q'}}[X^{q'}]$. However, this cancellation is never complete, leaving an error that cannot be made to vanish when models are trained independently.

For this reason, a single model capable of handling multiple charge states is required, as this ensures size-consistency by construction. As the defects of interest in the present work are deep, they are spatially localized. It is therefore sufficient to encode only the local effects introduced by the defect, rather than its effect on the entire supercell [49]. This can be achieved by training a model that distinguishes between bulk atoms and those neighboring a defect. The most natural way to implement this is to tag the nearest neighbors of a defect as a distinct atomic species, separate from the bulk, as illustrated in Fig. 4.1 where atoms closest to a vacancy are marked.

Several considerations are necessary to ensure consistent results from these models. The most important concerns how finite-size corrections are applied. The correction

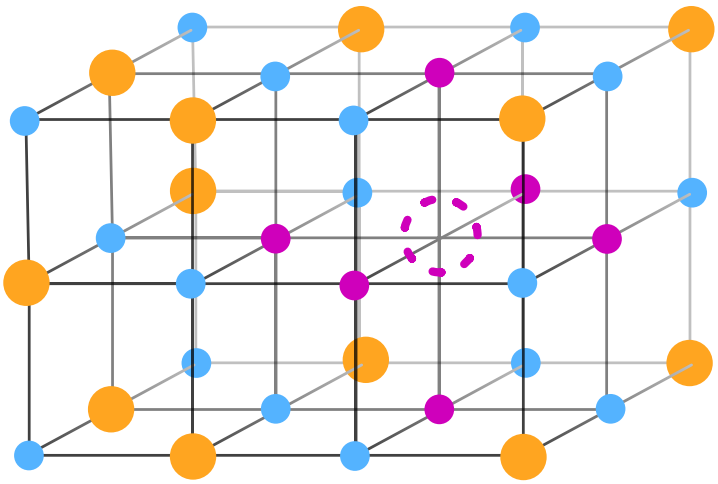

Figure 4.1: Illustration of atoms neighboring a vacancy being marked.

term E_{corr}, which is necessary for charged systems, can either be incorporated into the training data or applied to the model predictions afterward. In **PAPER III**, the latter approach was adopted. Since E_{corr} depends on system size, a consistent training procedure is required. Energies should therefore only be trained on charged structures containing a fixed number of atoms, while structures of other sizes only contribute with forces. This ensures that all training energies carry the same finite-size correction, which can then be applied to MLP predictions as a constant offset.

4.3 Molecular dynamics

With the PES in hand, either from DFT or a NEP model, we are now equipped to study the behavior of a crystal structure. Determining properties such as lattice parameters, heat capacities, or diffusion coefficients analytically is rarely feasible, and numerical sampling methods are therefore required. Material properties are obtained by sampling the system under well-defined thermodynamic conditions, such as fixed temperature, pressure, and particle number, with statistical averages over the sampled configurations yielding the desired observables. The central challenge is to generate configurations that are representative of the thermodynamic state of interest. MD addresses this by sampling phase space through explicit time propagation of the atomic degrees of freedom, with trajectories obtained by integrating Newton's equations of motion using forces derived from the underlying PES. Combined with a thermostat and barostat, this allows a physical system to be simulated under controlled temperature and pressure conditions.

Given a particle i, Newton's second law states that,

$$\mathbf{v}_i(t) = \frac{\mathrm{d}\mathbf{R}_i(t)}{\mathrm{d}t}, \quad \mathbf{a}_i(t) = \frac{\mathrm{d}\mathbf{v}_i(t)}{\mathrm{d}t} = \frac{\mathbf{F}_i(t)}{m_i} \tag{4.14}$$

where the forces are obtained from the PES by,

$$\mathbf{F}_i(\{\mathbf{R}(t)\}) = -\nabla_i U(\{\mathbf{R}(t)\}). \tag{4.15}$$

The difficult part of this is evaluating the PES. However, we have already established two ways of calculating this, by DFT in Sect. 4.1 and by a NEP model in Sect. 4.2.

With a method of evaluating the forces acting on each atom, we should now be able to evolve our atomic positions, $\{\mathbf{R}(t)\}$, in time. We have a choice to make in how we are going to solve Eq. (4.14) to propagate our MD simulation. The standard practice is to use the velocity Verlet algorithm [66],

$$\mathbf{R}_i(t + \Delta t) = \mathbf{R}_i(t) + \mathbf{v}_i(t)\Delta t + \frac{1}{2}\mathbf{a}_i(t)\Delta t^2, \tag{4.16}$$

$$\mathbf{a}_i(t + \Delta t) = \frac{1}{m}\mathbf{F}_i\left(\{\mathbf{R}(t + \Delta t)\}\right), \tag{4.17}$$

$$\mathbf{v}_i(t + \Delta t) = \mathbf{v}_i(t) + \frac{1}{2}\left(\mathbf{a}_i(t) + \mathbf{a}_i(t + \Delta t)\right)\Delta t, \tag{4.18}$$

which is a method that provides good numerical stability. Note that we still have to choose a sufficiently small time-step to obtain converged simulations. As a general guideline, the time-step should be picked in a way that the fastest frequency in your system is sampled several times during a period.

4.4 Thermodynamic integration

To perform the calculations necessary for modeling defects, discussed in Sect. 3.1, we need to obtain formation free energies. However, evaluating the free energy of a crystal structure at finite temperatures is non-trivial. The free energy depends on the partition function, which in principle requires sampling the entire phase space, an infeasible task for most systems. However, TI offers a practical route forward by instead computing the free energy difference between two systems with potential energies U_1 and U_2, which is a considerably more tractable problem. In some cases, such as when comparing two defect charge states, this difference is all that is needed. When the absolute free energy is required, it can be obtained by connecting to a reference system with a known analytical free energy, which is discussed later in this section.

TI is based on parameterizing a path between the two potentials, creating a new effective potential which for example could take the form: $U(\mathbf{\Gamma}; \lambda) = (1 - \lambda)U_1(\mathbf{\Gamma}) + \lambda U_2(\mathbf{\Gamma})$,

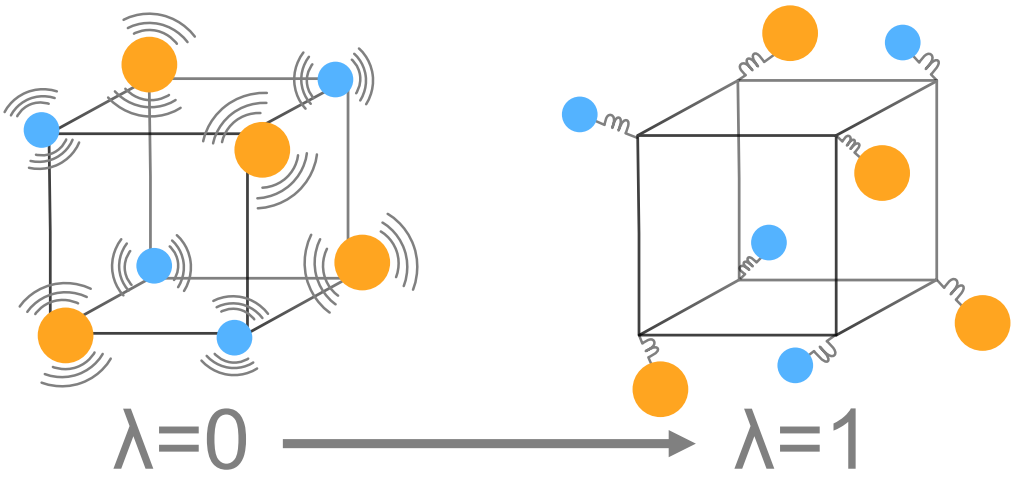

Figure 4.2: Illustration of how the atomic dynamics evolve as λ is varied. For $\lambda = 0$, the system is fully anharmonic (e.g., described by a MLP model), whereas for $\lambda = 1$, it reduces to an Einstein crystal in which each atom is harmonically bound to its lattice site.

where $\mathbf{\Gamma}$ is a point in phase space and λ is the parameter responsible for switching between the different potentials. Setting $\lambda = \lambda_i = 0$ yields U_1 and $\lambda = \lambda_f = 1$ yields U_2. For example, we can switch between a MLP model and an Einstein crystal, a reference system in which each atom is bound to its equilibrium position by a harmonic spring. At the endpoints, λ_i and λ_f, the potential energy is described fully by one of the two, while during the switch it is described by a mixture of the two, interpolating from a fully anharmonic potential to a harmonic one, as illustrated in Fig. 4.2.

The derivation of the free energy difference between two potentials starts from the partition function $\mathcal{Q}(\lambda)$ of the mixed potential, defined as [67],

$$\mathcal{Q}(\lambda) = \frac{1}{\Lambda^{3N} N!} \int \mathrm{d}\mathbf{\Gamma} \mathrm{e}^{-\beta U(\mathbf{\Gamma};\lambda)}, \tag{4.19}$$

where Λ is the thermal de Broglie wavelength, N is the number of particles, and $\beta = 1/(k_\mathrm{B}T)$ is the inverse thermal energy with k_B the Boltzmann constant. Since the free energy is obtained through $F(\lambda) = -\frac{1}{\beta}\ln[\mathcal{Q}(\lambda)]$, the derivative of our free energy with respect to λ can be expressed as an ensemble average since,

$$\begin{aligned}\frac{\partial F(\lambda)}{\partial \lambda} &= -\frac{1}{\beta}\frac{\partial}{\partial \lambda}\ln[\mathcal{Q}(\lambda)] = -\frac{1}{\beta}\frac{1}{\mathcal{Q}(\lambda)}\frac{\partial \mathcal{Q}(\lambda)}{\partial \lambda} = \\ &= \frac{\int \mathrm{d}\mathbf{\Gamma}(\partial U(\mathbf{\Gamma};\lambda)/\partial\lambda)\mathrm{e}^{-\beta U(\mathbf{\Gamma};\lambda)}}{\int \mathrm{d}\mathbf{\Gamma}\mathrm{e}^{-\beta U(\mathbf{\Gamma};\lambda)}} = \left\langle \frac{\partial U(\mathbf{\Gamma};\lambda)}{\partial \lambda} \right\rangle_{\lambda}.\end{aligned} \tag{4.20}$$

This means that we can express the change in free energy along the path $\lambda_i \to \lambda_f$ as [68],

$$\Delta F = F(\lambda_f) - F(\lambda_i) = \int_{\lambda_i}^{\lambda_f} \mathrm{d}\lambda \frac{\partial F(\lambda)}{\partial \lambda} = \int_{\lambda_i}^{\lambda_f} \mathrm{d}\lambda \left\langle \frac{\partial U(\mathbf{\Gamma};\lambda)}{\partial \lambda} \right\rangle_{\lambda}. \tag{4.21}$$

The change in free energy is also defined as the reversible work, W_{rev}, performed along the path. Evaluating the the free energy difference using this method requires performing several equilibrium simulations at discrete points along the integration path, typically by means of MD. While straightforward, this procedure can be computationally demanding due to the need for multiple independent runs. However, this approach can be extended to non-equilibrium simulations, allowing the free-energy difference to be evaluated from a single continuous MD simulation [69]. This is done by considering the paths $\lambda_i \to \lambda_f$ and $\lambda_f \to \lambda_i$, from which one can write the free energy difference as,

$$\Delta F = \frac{1}{2} W_{\mathrm{rev}}^{\lambda_i \to \lambda_f} - \frac{1}{2} W_{\mathrm{rev}}^{\lambda_f \to \lambda_i}. \tag{4.22}$$

The average irreversible work performed along a given path can be decomposed as $\langle W_{\mathrm{irr}} \rangle = W_{\mathrm{rev}} + \langle E_{\mathrm{dis}} \rangle$, where E_{dis} denotes the dissipated heat along the path. The ensemble averages are included to account for the varying initial conditions possible after equilibration [70]. If we switch λ slowly enough to remain close to the quasi-static limit, linear-response theory applies. In this regime, the system stays near equilibrium throughout the switching process, and the dissipated heat becomes equal in both directions, $E_{\mathrm{dis}}^{\lambda_i \to \lambda_f} = E_{\mathrm{dis}}^{\lambda_f \to \lambda_i}$, since the same amount of energy is dissipated regardless of the direction of the switch [71]. Due to this, we can rewrite Eq. (4.22) as,

$$\begin{aligned}\Delta F &= \frac{1}{2} W_{\mathrm{rev}}^{\lambda_i \to \lambda_f} - \frac{1}{2} W_{\mathrm{rev}}^{\lambda_f \to \lambda_i} \\ &= \frac{1}{2}\left(\left\langle W_{\mathrm{irr}}^{\lambda_i \to \lambda_f} \right\rangle - \left\langle E_{\mathrm{dis}}^{\lambda_i \to \lambda_f} \right\rangle\right) - \frac{1}{2}\left(\left\langle W_{\mathrm{irr}}^{\lambda_f \to \lambda_i} \right\rangle - \left\langle E_{\mathrm{dis}}^{\lambda_f \to \lambda_i} \right\rangle\right) \\ &= \frac{1}{2}\left(\left\langle W_{\mathrm{irr}}^{\lambda_i \to \lambda_f} \right\rangle - \left\langle E_{\mathrm{dis}}^{\lambda_i \to \lambda_f} \right\rangle\right) - \frac{1}{2}\left(\left\langle W_{\mathrm{irr}}^{\lambda_f \to \lambda_i} \right\rangle - \left\langle E_{\mathrm{dis}}^{\lambda_i \to \lambda_f} \right\rangle\right) \\ &= \frac{1}{2}\left\langle W_{\mathrm{irr}}^{\lambda_i \to \lambda_f} \right\rangle - \frac{1}{2}\left\langle W_{\mathrm{irr}}^{\lambda_f \to \lambda_i} \right\rangle.\end{aligned} \tag{4.23}$$

Introducing a time-dependence to our switching parameter, $\lambda = \lambda(t)$, allows for evaluation of the irreversible work along a non-equilibrium trajectory by evaluating,

$$W_{\text{irr}}^{\lambda_i \to \lambda_f} = \int_0^{t_f} \mathrm{d}t \frac{\mathrm{d}\lambda}{\mathrm{d}t} \frac{\partial U(\lambda)}{\partial \lambda}, \tag{4.24}$$

where t_f is the time of the simulation. Discretizing Eq. (4.24) and performing simulations along paths in both directions, $\lambda_i \to \lambda_f$ and $\lambda_f \to \lambda_i$, allows for accurate evaluation of Eq. (4.23) if simulation time is long enough for linear-response theory to apply.

This can be used out of the box to obtain free energy differences between different potential energy functions. Furthermore, the approach can be combined with systems that have analytically known free energies, such as the Einstein crystal for solids [72], the Uhlenbeck-Ford model for liquids [73] or the ideal gas for gases. By performing TI between an arbitrary potential energy to an appropriate systems with analytically known free energy allows for the absolute free energy of our arbitrary system to be found through,

$$F_{\text{arbitrary}} = F_{\text{analytical}} + \Delta F. \tag{4.25}$$

Care must however be taken when integrating along the path between two potentials, as events such as phase transitions may occur along the paths $\lambda_i \to \lambda_f$ and $\lambda_f \to \lambda_i$, in which case the evaluated free energy difference no longer corresponds to that of the intended initial structure. Therefor, careful consideration of the events that may occur along a path is required.

TI was employed in **PAPER III** to evaluate the thermodynamics of charged defects at finite temperature. This was carried out using two methods. The first method was based on obtaining the absolute free energies of both the pristine and defect-containing crystal structures by performing TI with an Einstein crystal as reference. These absolute free energies were subsequently inserted into Eq. (3.1) to obtain the defect formation free energies, which were then used in Eq. (3.3) to determine the CTLs. In the second method, we performed TI directly between defective crystal structures in different charge states. This enabled a direct evaluation of Eq. (3.3), bypassing the intermediate step of separately computing absolute free energies for each charge state. Direct thermodynamic integration between different charge states exhibits fast convergence relative to the method of obtaining the absolute free energies. This is most likely due to the relatively small free energy difference between the two charge states. In contrast, when computing absolute free energies via integration to a reference system such as the Einstein crystal, the associated free energy differences are substantially larger. Consequently, the integration requires longer simulations to achieve comparable convergence.

5

Summary of papers

Paper I

A morphotropic phase boundary in $MA_{1-x}FA_xPbI_3$: linking structure, dynamics, and electronic properties

The phase diagram of the mixed-cation halide perovskite $MA_{1-x}FA_xPbI_3$ was mapped using a machine-learned potential (MLP) combined with molecular dynamics (MD) simulations. The resulting phase diagram reconciles several experimental studies that previously lacked a consistent overall interpretation. A morphotropic phase boundary (MPB) was identified at approximately 27% FA content, marking the transition between out-of-phase and in-phase octahedral tilt patterns. This boundary coincides with a crossover of the M and R phonon modes, whose free energy landscapes become nearly degenerate at this composition. Close to the MPB, structures with layers of alternating tilt patterns emerge, illustrating a possible transition pathway across the boundary. Furthermore, density-functional theory (DFT) calculations reveal that band-edge fluctuations peak near the MPB, suggesting enhanced electron–phonon coupling. These findings establish a direct link between phonon dynamics, phase behavior, and electronic structure in mixed-cation perovskites.

Paper II

Revealing the Low-Temperature Phase of $FAPbI_3$ Using a Machine-Learned Potential

The low-temperature γ-phase of formamidinium lead iodide ($FAPbI_3$) was investigated using a MLP combined with large-scale MD simulations. The thermodynamic ground

state adopts an $a^-b^-b^-$ tilt pattern, with a high degree of orientational order among the organic FA cations. Upon cooling from the cubic phase, however, the system becomes kinetically trapped in a metastable $a^-a^-c^+$ configuration. This behavior arises from the first-order character of the transition into the $a^-b^-b^-$ phase, together with the freezing of the FA molecules into a disordered configuration. This provides a compelling microscopic explanation for the structural disorder observed experimentally in the low-temperature phase.

Paper III

Thermal Stabilization of Defect Charge States and Finite-Temperature Charge Transition Levels

A general finite-temperature framework for computing defect charge transition levels (CTLs) was introduced. It combines DFT-trained neuroevolution potential (NEP) models with thermodynamic integration (TI). The framework was applied to vacancies in MgO, LiF, and $CsSnBr_3$, where the temperature dependence of CTLs was decomposed into vibrational and band-edge contributions. The CTLs were found to shift substantially with temperature in all three materials, with direct implications for carrier concentrations and recombination dynamics. Notably, in $CsSnBr_3$, a neutral charge state becomes thermodynamically stable above 60 K, a behavior entirely absent at zero kelvin. Taken together, these results demonstrate that the widely used static, zero-kelvin defect formalism can miss both quantitative shifts in CTLs and the qualitative emergence of new stable charge states, underscoring the need to incorporate finite-temperature effects in predictive defect modeling.

6

Outlook

This thesis has investigated finite-temperature effects in semiconductors at the atomistic level, with a particular focus on halide perovskite-based materials. The central tool throughout has been machine-learned potential (MLP) models based on the neuroevolution potential (NEP) framework, which provide density-functional theory (DFT)-level accuracy at a fraction of the computational cost, thereby enabling the extensive configurational sampling required to capture thermal effects. These models were combined with molecular dynamics (MD) simulations and thermodynamic integration (TI) to examine two classes of phenomena: structural phase behavior in halide perovskites and the thermodynamics of charged point defects.

A natural continuation of **PAPER I** is to extend the compositional study to related mixed-cation systems or three-component alloys. If a mixed system have distinct phases for its boundary compositions, at least one morphotropic phase boundary (MPB) is inevitable in its phase diagram. Exploring such systems may help identify compositions where functional properties peak. The MLP-based methodology employed here is well suited to this task, given that the compositional space is too large to map using DFT alone.

In **PAPER II**, the kinetic trapping observed in $FAPbI_3$ raises broader questions about the role of cooling rate and sample preparation in determining the experimentally accessible phases of organic-inorganic perovskites. Future work could quantify the energy barriers separating competing low-temperature phases to estimate the timescales over which the metastable phase relaxes. This would provide a direct link between simulation and the thermal annealing protocols used experimentally.

The finite-temperature defect framework introduced in **PAPER III** could be extended in several directions. The current study is limited to vacancies; extending it to interstitial and substitutional defects would give a more complete picture of defect thermodynamics in the materials studied. Furthermore, only a small set of semiconductors has

been considered here and systematic application of the framework to a broader class of photovoltaic-relevant materials.

More broadly, the results presented in this thesis suggest that finite-temperature modeling is a crucial component of computational materials workflow for photovoltaic applications. As MLP models continue to improve in accuracy, it is anticipated that temperature-dependent properties will become routinely accessible quantities for a wide range of technologically relevant semiconductors.

Acknowledgments

I would like to thank my supervisor, Julia Wiktor, for her guidance and support throughout this work. I greatly appreciate the knowledge she has shared, the trust she has placed in my abilities and how quickly she replies whenever I have a question.

I am also thankful to my co-supervisor, Paul Erhart, for his valuable insights and for the many helpful reminders about condensed matter theory.

I would also like to thank my examiner, Andreas Isacsson, for his valuable feedback and support.

My thanks go as well to my colleagues in Condensed Matter and Materials Theory for creating an enjoyable working environment.

Finally, I am deeply grateful to my family and friends for their support.

Bibliography

[1] C. S. Ponseca, T. J. Savenije, M. Abdellah, K. Zheng, A. Yartsev, T. Pascher, T. Harlang, P. Chabera, T. Pullerits, A. Stepanov, J.-P. Wolf, and V. Sundström, *Organometal Halide Perovskite Solar Cell Materials Rationalized: Ultrafast Charge Generation, High and Microsecond-Long Balanced Mobilities, and Slow Recombination,* Journal of the American Chemical Society **136**, 5189 (2014). doi:10.1021/ja412583t.

[2] E. Edri, S. Kirmayer, S. Mukhopadhyay, K. Gartsman, G. Hodes, and D. Cahen, *Elucidating the charge carrier separation and working mechanism of $CH_3NH_3PbI_{3-x}Cl_x$ perovskite solar cells,* Nature Communications **5**, 3461 (2014). doi:10.1038/ncomms4461.

[3] Y. Bi, E. M. Hutter, Y. Fang, Q. Dong, J. Huang, and T. J. Savenije, *Charge Carrier Lifetimes Exceeding* 15 µs *in Methylammonium Lead Iodide Single Crystals,* The Journal of Physical Chemistry Letters **7**, 923 (2016). doi:10.1021/acs.jpclett.6b00269.

[4] G. Kim and A. Petrozza, *Defect Tolerance and Intolerance in Metal-Halide Perovskites,* Advanced Energy Materials **10**, 2001959 (2020). doi:10.1002/aenm.202001959.

[5] J. Kang and L.-W. Wang, *High Defect Tolerance in Lead Halide Perovskite $CsPbBr_3$,* The Journal of Physical Chemistry Letters **8**, 489 (2017). doi:10.1021/acs.jpclett.6b02800.

[6] A. K. Jena, A. Kulkarni, and T. Miyasaka, *Halide perovskite photovoltaics: Background, status, and future prospects,* Chemical Reviews **119**, 3036 (2019). doi:10.1021/acs.chemrev.8b00539.

[7] *Best Research-Cell Efficiency Chart,* https://www.nrel.gov/pv/cell-efficiency.html; accessed: 2026-04-15.

[8] L. Zhang, L. Mei, K. Wang, Y. Lv, S. Zhang, Y. Lian, X. Liu, Z. Ma, G. Xiao, Q. Liu, S. Zhai, S. Zhang, G. Liu, L. Yuan, B. Guo, Z. Chen, K. Wei, A. Liu, S. Yue, G. Niu, X. Pan, J. Sun, Y. Hua, W.-Q. Wu, D. Di, B. Zhao, J. Tian, Z. Wang, Y. Yang, L. Chu, M. Yuan, H. Zeng, H.-L. Yip, K. Yan, W. Xu, L. Zhu, W. Zhang, G. Xing, F. Gao, and L. Ding, *Advances in the Application of Perovskite Materials,* Nano-Micro Letters **15**, 177 (2023). doi:10.1007/s40820-023-01140-3.

[9] Q. Chen, N. De Marco, Y. M. Yang, T.-B. Song, C.-C. Chen, H. Zhao, Z. Hong, H. Zhou, and Y. Yang, *Under the spotlight: The organic–inorganic hybrid halide perovskite for optoelectronic applications,* Nano Today **10**, 355 (2015). doi:https://doi.org/10.1016/j.nantod.2015.04.009.

[10] S.-H. Jeong, J. Park, T.-H. Han, F. Zhang, K. Zhu, J. S. Kim, M.-H. Park, M. O. Reese, S. Yoo, and T.-W. Lee, *Characterizing the Efficiency of Perovskite Solar Cells and Light-Emitting Diodes,* Joule **4**, 1206 (2020). doi:https://doi.org/10.1016/j.joule.2020.04.007.

[11] Z. A. VanOrman and L. Nienhaus, *Recent advancements in halide perovskite nanomaterials and their optoelectronic applications,* InfoMat **3**, 962 (2021). doi:https://doi.org/10.1002/inf2.12187.

[12] M. Morana, J. Wiktor, M. Coduri, R. Chiara, C. Giacobbe, E. L. Bright, F. Ambrosio, F. De Angelis, and L. Malavasi, *Cubic or Not Cubic? Combined Experimental and Computational Investigation of the Short-Range Order of Tin Halide Perovskites,* The Journal of Physical Chemistry Letters **14**, 2178 (2023). PMID: 36808992. doi:10.1021/acs.jpclett.3c00105.

[13] A. M. Glazer, *The classification of tilted octahedra in perovskites,* Acta Crystallographica Section B: Structural Crystallography and Crystal Chemistry **28**, 3384 (1972). doi:10.1107/S0567740872007976.

[14] A. Mohanty, D. Swain, S. Govinda, T. N. G. Row, and D. D. Sarma, *Phase Diagram and Dielectric Properties of $MA_{1-x}FA_xPbI_3$,* ACS Energy Letters **4**, 2045 (2019). doi:10.1021/acsenergylett.9b01291.

[15] M. Simenas, A. Gagor, J. Banys, and M. Maczka, *Phase Transitions and Dynamics in Mixed Three- and Low-Dimensional Lead Halide Perovskites,* Chemical Reviews **124**, 2281 (2024). doi:10.1021/acs.chemrev.3c00532.

[16] N. K. Noel, S. N. Habisreutinger, B. Wenger, M. T. Klug, M. T. Hörantner, M. B. Johnston, R. J. Nicholas, D. T. Moore, and H. J. Snaith, *A low viscosity, low boiling point, clean solvent system for the rapid crystallisation of highly specular perovskite films,* Energy Environ. Sci. **10**, 145 (2017). doi:10.1039/C6EE02373H.

[17] Q. Chen, H. Zhou, Z. Hong, S. Luo, H.-S. Duan, H.-H. Wang, Y. Liu, G. Li, and Y. Yang, *Planar Heterojunction Perovskite Solar Cells via Vapor-Assisted Solution Process,* Journal of the American Chemical Society **136**, 622 (2014). doi:10.1021/ja411509g.

[18] H. Shahivandi, *Understanding thermal effects on band gap and absorption in MAPbI3 perovskite solar cells,* Solid State Sciences **168**, 108054 (2025). doi:https://doi.org/10.1016/j.solidstatesciences.2025.108054.

[19] R. L. Milot, G. E. Eperon, H. J. Snaith, M. B. Johnston, and L. M. Herz, *Temperature-Dependent Charge-Carrier Dynamics in $CH_3NH_3PbI_3$ Perovskite Thin Films,* Advanced Functional Materials **25**, 6218 (2015). doi:https://doi.org/10.1002/adfm.201502340.

[20] C. Quarti, E. Mosconi, J. M. Ball, V. D'Innocenzo, C. Tao, S. Pathak, H. J. Snaith, A. Petrozza, and F. De Angelis, *Structural and optical properties of methylammonium lead iodide across the tetragonal to cubic phase transition: implications for perovskite solar cells,* Energy Environ. Sci. **9**, 155 (2016). doi:10.1039/C5EE02925B.

[21] A. Francisco-López, B. Charles, M. I. Alonso, M. Garriga, M. Campoy-Quiles, M. T. Weller, and A. R. Goñi, *Phase Diagram of Methylammonium/Formamidinium Lead Iodide Perovskite Solid Solutions from Temperature-Dependent Photoluminescence and Raman Spectroscopies,* The Journal of Physical Chemistry C **124**, 3448 (2020). doi:10.1021/acs.jpcc.9b10185.

[22] E. Fransson, J. M. Rahm, J. Wiktor, and P. Erhart, *Revealing the Free Energy Landscape of Halide Perovskites: Metastability and Transition Characters in $CsPbBr_3$ and $MAPbI_3$,* Chemistry of Materials **35**, 8229 (2023). doi:10.1021/acs.chemmater.3c01740.

[23] T. T. Ava, A. Al Mamun, S. Marsillac, and G. Namkoong, *A Review: Thermal Stability of Methylammonium Lead Halide Based Perovskite Solar Cells,* Applied Sciences **9**, 188 (2019). doi:10.3390/app9010188.

[24] Z. Qiu, N. Li, Z. Huang, Q. Chen, and H. Zhou, *Recent Advances in Improving Phase Stability of Perovskite Solar Cells,* Small Methods **4**, 1900877 (2020). doi:10.1002/smtd.201900877.

[25] Y. Li, A. Bahnick, P. J. Lohr, S. Raglow, and A. D. Printz, *Enhanced α-phase stability of formamidinium lead iodide with addition of 5-ammonium valeric acid chloride,* Energy Advances **4**, 262 (2024). doi:10.1039/D4YA00527A.

[26] T. Niu, L. Chao, X. Dong, L. Fu, and Y. Chen, *Phase-Pure α-$FAPbI_3$ for Perovskite Solar Cells,* The Journal of Physical Chemistry Letters **13**, 1845 (2022). doi:10.1021/acs.jpclett.1c04241.

[27] Z. Zheng, S. Wang, Y. Hu, Y. Rong, A. Mei, and H. Han, *Development of formamidinium lead iodide-based perovskite solar cells: efficiency and stability,* Chemical Science **13**, 2167 (2022). doi:10.1039/D1SC04769H.

[28] D. H. Fabini, T. A. Siaw, C. C. Stoumpos, G. Laurita, D. Olds, K. Page, J. G. Hu, M. G. Kanatzidis, S. Han, and R. Seshadri, *Universal Dynamics of Molecular Reorientation in Hybrid Lead Iodide Perovskites,* Journal of the American Chemical Society **139**, 16875 (2017). doi:10.1021/jacs.7b09536.

[29] P. Tuo, L. Li, X. Wang, J. Chen, Z. Zhong, B. Xu, and F.-Z. Dai, *Spontaneous Hybrid Nano-Domain Behavior of the Organic–Inorganic Hybrid Perovskites,* Adv. Funct. Mater. **33**, 2301663 (2023). doi:10.1002/adfm.202301663.

[30] R. Lavén, M. M. Koza, L. Malavasi, A. Perrichon, M. Appel, and M. Karlsson, *Rotational Dynamics of Organic Cations in Formamidinium Lead Iodide Perovskites,* The Journal of Physical Chemistry Letters **14**, 2784 (2023). doi:10.1021/acs.jpclett.3c00185.

[31] C. C. Stoumpos, C. D. Malliakas, and M. G. Kanatzidis, *Semiconducting Tin and Lead Iodide Perovskites with Organic Cations: Phase Transitions, High Mobilities, and Near-Infrared Photoluminescent Properties,* Inorganic Chemistry **52**, 9019 (2013). doi:10.1021/ic401215x.

[32] K. Drużbicki, R. Lavén, J. Armstrong, L. Malavasi, F. Fernandez-Alonso, and M. Karlsson, *Cation Dynamics and Structural Stabilization in Formamidinium Lead Iodide Perovskites,* The Journal of Physical Chemistry Letters **12**, 3503 (2021). PMID: 33792334. doi:10.1021/acs.jpclett.1c00616.

[33] B. Charles, J. Dillon, O. J. Weber, M. S. Islam, and M. T. Weller, *Understanding the stability of mixed A-cation lead iodide perovskites,* Journal of Materials Chemistry A **5**, 22495 (2017). doi:10.1039/C7TA08617B.

[34] A. P. S. S. K. Mishra and D. Pandey, *Thermodynamic nature of phase transitions in $Pb(Zr_xTi_{1-x})O_3$ ceramics near the morphotropic phase boundary. I. Structural studies,* Philosophical Magazine B **76**, 213 (1997). doi:10.1080/01418639708241086.

[35] B. Noheda, D. E. Cox, G. Shirane, J. A. Gonzalo, L. E. Cross, and S.-E. Park, *A monoclinic ferroelectric phase in the $Pb(Zr_{1-x}Ti_x)O_3$ solid solution,* Applied Physics Letters **74**, 2059 (1999). doi:10.1063/1.123756.

[36] O. J. Weber, B. Charles, and M. T. Weller, *Phase behaviour and composition in the formamidinium–methylammonium hybrid lead iodide perovskite solid solution,* J. Mater. Chem. A **4**, 15375 (2016). doi:10.1039/C6TA06607K.

[37] H. Zheng, J. Dai, J. Duan, F. Chen, G. Zhu, F. Wang, and C. Xu, *Temperature-dependent photoluminescence properties of mixed-cation methylammonium–formamidium lead iodide $[HC(NH_2)_2]_x[CH_3NH_3]_{1-x}PbI_3$ perovskite nanostructures,* J. Mater. Chem. C **5**, 12057 (2017). doi:10.1039/C7TC04146B.

[38] R. Phillips, *Crystals, Defects and Microstructures: Modeling Across Scales* (Cambridge University Press, 2001). ISBN 9780521790055 9780521793575 9780511606236. doi:10.1017/CBO9780511606236.

[39] C. Freysoldt, B. Grabowski, T. Hickel, J. Neugebauer, G. Kresse, A. Janotti, and C. G. Van de Walle, *First-principles calculations for point defects in solids,* Rev. Mod. Phys. **86**, 253 (2014). doi:10.1103/RevModPhys.86.253.

[40] C. Linderälv, A. Lindman, and P. Erhart, *A Unifying Perspective on Oxygen Vacancies in Wide Band Gap Oxides,* The Journal of Physical Chemistry Letters **9**, 222 (2018). PMID: 29265821. doi:10.1021/acs.jpclett.7b03028.

[41] C. Hellenthal, R. Heimbuch, K. Sotthewes, E. S. Kooij, and H. J. W. Zandvliet, *Determining the local density of states in the constant current STM mode,* Phys. Rev. B **88**, 035425 (2013). doi:10.1103/PhysRevB.88.035425.

[42] M. M. Roessler and E. Salvadori, *Principles and applications of EPR spectroscopy in the chemical sciences,* Chem. Soc. Rev. **47**, 2534 (2018). doi:10.1039/C6CS00565A.

[43] F. Selim, *Positron annihilation spectroscopy of defects in nuclear and irradiated materials- a review,* Materials Characterization **174**, 110952 (2021). doi:https://doi.org/10.1016/j.matchar.2021.110952.

[44] S. A. Bonke, T. Risse, A. Schnegg, and A. Brückner, *In situ electron paramagnetic resonance spectroscopy for catalysis,* Nature Reviews Methods Primers **1**, 33 (2021). doi:10.1038/s43586-021-00031-4.

[45] A. Langørgen, L. Vines, and Y. Kalmann Frodason, *Perspective on electrically active defects in β-Ga_2O_3 from deep-level transient spectroscopy and first-principles calculations,* Journal of Applied Physics **135**, 195702 (2024). doi:10.1063/5.0205950.

[46] C. Freysoldt, J. Neugebauer, and C. G. Van de Walle, *Fully Ab Initio Finite-Size Corrections for Charged-Defect Supercell Calculations,* Phys. Rev. Lett. **102**, 016402 (2009). doi:10.1103/PhysRevLett.102.016402.

[47] C. Freysoldt, J. Neugebauer, and C. G. Van de Walle, *Electrostatic interactions between charged defects in supercells,* physica status solidi (b) **248**, 1067 (2011). doi:https://doi.org/10.1002/pssb.201046289.

[48] I. Mosquera-Lois, S. R. Kavanagh, J. Klarbring, K. Tolborg, and A. Walsh, *Imperfections are not 0 K: free energy of point defects in crystals,* Chem. Soc. Rev. **52**, 5812 (2023). doi:10.1039/D3CS00432E.

[49] C. Linderälv, A. Lindman, and P. Erhart, *A Unifying Perspective on Oxygen Vacancies in Wide Band Gap Oxides,* The Journal of Physical Chemistry Letters **9**, 222 (2018). doi:10.1021/acs.jpclett.7b03028.

[50] I. Mosquera-Lois and A. Walsh, *Dynamic Vacancy Levels in $CsPbCl_3$ Obey Equilibrium Defect Thermodynamics,* PRX Energy **4**, 043008 (2025). doi:10.1103/dxmb-8s96.

[51] R. A. Redkin, N. I. Onishchenko, A. V. Kosobutsky, V. N. Brudnyi, X. Su, and S. Y. Sarkisov, *Temperature-Dependent Optical Absorption and DLTS Study of As-Grown and Electron-Irradiated GaSe Crystals,* Crystals **15**, (2025). doi:10.3390/cryst15040372.

[52] E. Schrödinger, *Quantisierung als Eigenwertproblem,* Annalen der Physik **384**, 361 (1926). doi:10.1002/andp.19263840404.

[53] M. Born and R. Oppenheimer, *Zur Quantentheorie der Molekeln,* Annalen der Physik **389**, 457 (1927). doi:10.1002/andp.19273892002.

[54] F. Giustino, *Materials Modelling Using Density Functional Theory: Properties and Predictions* (Oxford University Press, 2014). ISBN 9780199662449. Google-Books-ID: FzOTAwAAQBAJ.

[55] P. Hohenberg and W. Kohn, *Inhomogeneous electron gas,* Physical Review **136**, B864 (1964). doi:10.1103/PhysRev.136.B864.

[56] W. Kohn and L. J. Sham, *Self-Consistent Equations Including Exchange and Correlation Effects,* Phys. Rev. **140**, A1133 (1965). doi:10.1103/PhysRev.140.A1133.

[57] J. P. Perdew, K. Burke, and M. Ernzerhof, *Generalized Gradient Approximation Made Simple,* Phys. Rev. Lett. **77**, 3865 (1996). doi:10.1103/PhysRevLett.77.3865.

[58] J. P. Perdew, A. Ruzsinszky, G. I. Csonka, O. A. Vydrov, G. E. Scuseria, L. A. Constantin, X. Zhou, and K. Burke, *Restoring the Density-Gradient Expansion for Exchange in Solids and Surfaces,* Phys. Rev. Lett. **100**, 136406 (2008). doi:10.1103/PhysRevLett.100.136406.

[59] J. Heyd, G. E. Scuseria, and M. Ernzerhof, *Hybrid functionals based on a screened Coulomb potential,* The Journal of Chemical Physics **118**, 8207 (2003). doi:10.1063/1.1564060.

[60] S. Klawohn, J. P. Darby, J. R. Kermode, G. Csányi, M. A. Caro, and A. P. Bartók, *Gaussian approximation potentials: Theory, software implementation and application examples,* The Journal of Chemical Physics **159**, 174108 (2023). doi:10.1063/5.0160898.

[61] B. Gurlek, S. Sharma, P. Lazzaroni, A. Rubio, and M. Rossi, *Accurate machine learning interatomic potentials for polyacene molecular crystals: application to single molecule host-guest systems,* npj Computational Materials **11**, 318 (2025). doi:10.1038/s41524-025-01825-w.

[62] K. Song, R. Zhao, J. Liu, Y. Wang, E. Lindgren, Y. Wang, S. Chen, K. Xu, T. Liang, P. Ying, N. Xu, Z. Zhao, J. Shi, J. Wang, S. Lyu, Z. Zeng, S. Liang, H. Dong, L. Sun, Y. Chen, Z. Zhang, W. Guo, P. Qian, J. Sun, P. Erhart, T. Ala-Nissila, Y. Su, and Z. Fan, *General-purpose machine-learned potential for 16 elemental metals and their alloys,* Nature Communications **15**, 10208 (2024). doi:10.1038/s41467-024-54554-x.

[63] Z. Fan, Y. Wang, P. Ying, K. Song, J. Wang, Y. Wang, Z. Zeng, K. Xu, E. Lindgren, J. M. Rahm, A. J. Gabourie, J. Liu, H. Dong, J. Wu, Y. Chen, Z. Zhong, J. Sun, P. Erhart, Y. Su, and T. Ala-Nissila, *GPUMD: A package for constructing accurate machine-learned potentials and performing highly efficient atomistic simulations,* The Journal of Chemical Physics **157**, 114801 (2022). doi:10.1063/5.0106617.

[64] K. Xu, H. Bu, S. Pan, E. Lindgren, Y. Wu, Y. Wang, J. Liu, K. Song, B. Xu, Y. Li, T. Hainer, L. Svensson, J. Wiktor, R. Zhao, H. Huang, C. Qian, S. Zhang, Z. Zeng, B. Zhang, B. Tang,

Y. Xiao, Z. Yan, J. Shi, Z. Liang, J. Wang, T. Liang, S. Cao, Y. Wang, P. Ying, N. Xu, C. Chen, Y. Zhang, Z. Chen, X. Wu, W. Jiang, E. Berger, Y. Li, S. Chen, A. J. Gabourie, H. Dong, S. Xiong, N. Wei, Y. Chen, J. Xu, F. Ding, Z. Sun, T. Ala-Nissila, A. Harju, J. Zheng, P. Guan, P. Erhart, J. Sun, W. Ouyang, Y. Su, and Z. Fan, *GPUMD 4.0: A high-performance molecular dynamics package for versatile materials simulations with machine-learned potentials,* Materials Genome Engineering Advances **3**, e70028 (2025). doi:https://doi.org/10.1002/mgea.70028.

[65] J. Behler, *Perspective: Machine learning potentials for atomistic simulations,* The Journal of Chemical Physics **145**, 170901 (2016). doi:10.1063/1.4966192.

[66] W. C. Swope, H. C. Andersen, P. H. Berens, and K. R. Wilson, *A computer simulation method for the calculation of equilibrium constants for the formation of physical clusters of molecules: Application to small water clusters,* The Journal of Chemical Physics **76**, 637 (1982). doi:10.1063/1.442716.

[67] D. Frenkel and B. Smit, *Understanding Molecular Simulation* (Elsevier, 2002). ISBN 9780122673511. doi:10.1016/B978-0-12-267351-1.X5000-7.

[68] D. Frenkel and A. J. C. Ladd, *New Monte Carlo method to compute the free energy of arbitrary solids. Application to the fcc and hcp phases of hard spheres,* The Journal of Chemical Physics **81**, 3188 (1984). doi:10.1063/1.448024.

[69] R. Freitas, M. Asta, and M. de Koning, *Nonequilibrium free-energy calculation of solids using LAMMPS,* Computational Materials Science **112**, 333 (2016). doi:https://doi.org/10.1016/j.commatsci.2015.10.050.

[70] C. Jarzynski, *Nonequilibrium Equality for Free Energy Differences,* Phys. Rev. Lett. **78**, 2690 (1997). doi:10.1103/PhysRevLett.78.2690.

[71] M. De Koning, *Optimizing the driving function for nonequilibrium free-energy calculations in the linear regime: A variational approach,* Journal of Chemical Physics **122**, (2005). Cited by: 47. doi:10.1063/1.1860556.

[72] D. Frenkel and A. J. C. Ladd, *New Monte Carlo method to compute the free energy of arbitrary solids. Application to the fcc and hcp phases of hard spheres,* The Journal of Chemical Physics **81**, 3188 (1984). doi:10.1063/1.448024.

[73] R. Paula Leite, R. Freitas, R. Azevedo, and M. de Koning, *The Uhlenbeck-Ford model: Exact virial coefficients and application as a reference system in fluid-phase free-energy calculations,* The Journal of Chemical Physics **145**, 194101 (2016). doi:10.1063/1.4967775.